AN INVESTIGATION OF MOLYBDENUM STEELS & WHITE IRONS FOR ABRASIVE WEAR RESISTANCE

Dale E. Christensen

B.S., Washington State University, 1981

A thesis submitted to the faculty of the
Oregon Graduate Institute of Science and Technology
in partial fulfillment of the
requirements for the degree of
Master of Science
in
Materials Science and Engineering

May 1997

The Thesis "An Investigation of Molybdenum Steels and White Irons for Abrasive Wear Resistance" by Dale E. Christensen, has been examined and approved by the following Examination Committee:

Paul Clayton, Professor
Thesis Advisor

Milton R. Scholl, Assistant Professor

Jim Stanley, Adjunct Professor

DEDICATION

In memorial to my mother, Catherine Helen Christensen, for her unwavering faith in my abilities and her boundless pride in my accomplishments.

ACKNOWLEDGMENTS

To Paul Clayton, my thesis advisor and employer, for the loyalty and support during my eleven years as a member of the Wear Group and part-time student at The Oregon Graduate Institute. Thank you for allowing me to pursue this project in spite of its constant diversion of my attention from our research effort. To Milt Scholl for his advice, guidance, and interest in my research. To Jim Stanley for his moral support and willingness to review this document.

A special thanks to all of the members of the Wear Group for their insight, support, and friendship and for making my career at The Oregon Graduate Institute a wonderful, enriching experience. I will always appreciate the genuine interest in my success and the many helpful discussions during the course of my work.

I would also like to thank ASM International, The American Society of Tribology and Lubrication Engineers, Elsevier Science, the publishers of The Wear Journal, Pergammon, Ltd., publisher of CALPHAD, and Carl Hanser Verlag, publisher of Zeitschrift fur Metallkunde, for allowing the use of copyrighted material in this thesis.

TABLE OF CONTENTS

LIST OF TABLES

LIST OF FIGURES

ABSTRACT

AN INVESTIGATION OF MOLYBDENUM STEELS & WHITE IRONS FOR ABRASIVE WEAR RESISTANCE

Dale E. Christensen

Supervising Professor: Dr. Paul Clayton

Many commercial hardfacing alloys rely on chromium carbides for their wear resistance. The objective of this work was to relate the abrasive wear behavior of molybdenum steels and white iron alloys, derived from the Iron-Molybdenum-Carbon ternary system, to their microstructure. The focus is on alternatives to conventional chromium alloys using molybdenum carbides instead of chromium carbides for abrasion resistance.

Very little work has been published examining high-carbon, high-molybdenum alloys of the Fe-Mo-C system. Most of the work was done prior to 1967 and the Fe-Mo-C phase diagram is still not well established. The major interest over the years has been in the carbides and intermetallic phases of iron and molybdenum which are developed in common tool steels.

For this investigation, a series of commercial high-chromium and experimental high-molybdenum alloys were investigated and compared. The chromium materials included samples sectioned from commercial sand castings and a wrought tool steel. The molybdenum alloys were produced from blended powders which were sintered and then melted in a small laboratory arc melt furnace. The melting was performed in a water cooled copper crucible which produced very fine microstructural constituents in the alloy. The hard phase materials contained in the alloys included molybdenum carbides and molybdenum-iron intermetallic compounds. Dry Sand Rubber Wheel tests were performed and the wear rates were related to bulk hardness, carbon content, the type of hard phases and carbide volume

fraction. Failure analysis was performed on the wear surfaces utilizing a scanning electron microscope to determine the predominant wear mechanisms. A combination of metallographic techniques and X-ray diffraction were used to identify the microconstituents of the experimental materials.

The commercial chromium alloys obtained a similar level of wear resistance with a lower carbide volume fraction than the experimental molybdenum materials. A sample of one cast commercial white iron was remelted in the arc melt furnace to produce fine microstructural constituents similar to that of the experimental molybdenum alloys. This change in the microstructure produced a substantial reduction in wear resistance in this case. The differences in wear resistance between the various alloys examined is explained by the relative size and spacing of the hard phases in the chromium and molybdenum materials and the relative wear characteristics of the intermetallic and carbidic hard phases.

CHAPTER 1.
INTRODUCTION

Strategic materials are those which are vital to economic and military interests and must be obtained through importation [1]. Scholl [2] studied the viability of wear resistant alloys with intermetallic compounds substituted for the typical carbidic hard phases found in most alloys of this type. The primary purpose of his work was to develop alternative hardfacing materials without using strategic elements for alloy additions. This project is an extension of some aspects of that work.

Some of the most common hardfacing alloys are the commercial white irons which rely primarily on chromium carbides of the M_7C_6 type for their wear resistance. These alloys provide excellent abrasive wear resistance in many different environments with additions of 15 to 25 wt% chromium. However, chromium is considered to be a strategic material [1]. The objective of this work was to relate the abrasive wear behavior of molybdenum steels and white iron alloys derived from the Iron-Molybdenum-Carbon (Fe-Mo-C) ternary system to their microstructures. The emphasis is on alternatives to conventional chromium white irons using molybdenum carbides instead of chromium carbides for abrasion resistance.

Very little work has been published examining high-carbon high-molybdenum alloys of the Fe-Mo-C system. Most of the work was done prior to 1967 and the Fe-Mo-C phase diagram is still not well established. The major interest over the years has been in the carbides and intermetallics of iron and molybdenum which are found in common tool steels. In these, the carbon content is rarely over 0.75 wt% and the molybdenum ranges up to 6 wt%. Literature concerning the abrasive wear resistance of molybdenum carbide containing white irons has not been found. This lack of data is not surprising in light of the excellent wear resistance provided by the established chromium white irons and the relatively high cost of molybdenum.

In spite of the negative economic aspects, there are some interesting properties for the molybdenum carbides that have been noted. Similar hardnesses are shown between the chromium and molybdenum carbides and the melting point of the molybdenum carbides are significantly higher, Table 1.1. The toxicity [3] of chromium is a concern to those who are welding, grinding, or melting alloys containing this element as are the environmental aspects of waste disposal.

Table 1.1: Properties of Carbides

Material	Microhardness (Kg/mm^2)	Melting Point (°C)
$Cr_{23}C_6$	1663 [4]	1518 [4]
Cr_7C_3	1882 [4]	1782 [4]
Cr_3C_2	1800 [4]	1895 [4]
Fe_3C	840 - 1100 [6]	1650 [4]
WC	2200 [4]	2770 [7]
VC	2800 [6]	2648 [4]
TiC	3200 [4,6]	3140 [7]
MoC	1500 [6,8]	2700 [8]
Mo_2C	1500 [6,7,8]	2690 [8]
Quartz Sand	900 - 1280 [5,6]	-

CHAPTER 2.
LITERATURE SEARCH

2.1 Molybdenum Carbides

One of the earliest reports on the Fe-Mo-C system was written by Takei in 1932 and discussed in Rivlin's critical review of the system [9]. Takei was working to establish the liquidus projection and isotherms for the system. Takei's 700°C isotherm displayed an $(Fe,Mo)_3C$ and an $(Fe,Mo)_6C$ carbide. At that time he determined the M_6C structure to be complex fcc and also had evidence of another triple carbide which he labeled the xi phase, ξ. Dyson and Andrews [10] discussed an Fe_mMo_nC carbide reported by Lashko and Nesterova in 1951 that was extracted from a molybdenum steel after tempering for 20 hours at 600°C. Kuo [11] found a carbide in 1953, which he called M_aC_b, in molybdenum steels of similar composition to that studied by Lashko and Nesterova. He was unsure of its nature but concluded that the M_aC_b composition was between that of the $M_{23}C_6$ and Mo_2C based on when the various carbides formed in the molybdenum steels. Using his prior experience with tungsten carbides, which have the same atomic ratios, he postulated that the M_aC_b carbide formed after the M_6C but before the $M_{23}C_6$ which was the point at which the Fe_3C carbide was found in his molybdenum steels.

In the 1953 publication, Kuo studied the solidification and transformation behavior of carbides on a series of chromium, molybdenum, and tungsten steels. He performed isothermal transformations at 700°C for various lengths of time and performed his analysis using X-ray powder diffraction. The difference between the tungsten and molybdenum systems was found to be the level of instability of some of the carbides after the isothermal transformation. The $M_{23}C_6$ and Mo_2C carbides were found to be unstable and degraded after 2000 hours. However, greater stability was found in the Mo_2C with respect to the W_2C. This

was determined from carburizing molybdenum powder with carbon dioxide where the Mo_2C did not disappear after prolonged carburization. The W_2C carbide would not form under the same conditions.

Kuo related the type of carbide that formed to the Mo:C atomic ratio of the alloy. He felt that the amount of substitution for an element was based on its availability. Carbide M_6C was found to have long term stability at an atomic ratio greater than 3. At a ratio between 2 and 3 the Fe_4Mo_2C and Fe_3Mo_3C carbides began to appear. The intermetallic Fe_7Mo_6 was found to appear after a Mo:Fe atomic ratio of 5 was reached. Kuo's Mo_6C carbides contained approximately 50 - 60 at% molybdenum.

In another 1953 publication, Kuo [12] described two general forms of the M_6C type carbide. The compositions for the two carbides were given as A_2B_4C and as a range between A_3B_3C - A_4B_2C where the A-atoms and B-atoms are randomly substituted in the crystal lattice. The A-atom is a transitional metal in period IV, such as iron, and the B-atom is a metal in the V or VI period, such as molybdenum. The B-atom is larger than the A-atom holding a position diagonally below and to the left in the periodic table. The ratio of atomic size for A-atoms and B-atoms is in the range of 1.10 to 1.18. Kuo found that the cubic crystal edge changed according to the composition of the material. The crystal size increased as a result of having more of the larger B-atoms. The Fe_2Mo_4C carbide was not found when iron was in excess. The atomic ratios for carbides in the Fe-Mo-C system are given in Table 2.1.

Campbell et al [13] assembled a phase diagram of the Fe-Mo-C system in 1959 showing M_3C, $M_{23}C_6$, M_6C, and Mo_2C in steels with up to 6 wt% molybdenum. They found nothing like the anonymous carbides described by Kuo or Lashko and Nesterova. Dyson and Andrews [10] in 1964 determined that Kuo's M_aC_b carbide and Lashko and Nesterova's Fe_mMo_nC were actually the Fe_2MoC carbide. They determined its structure to be orthorhombic and isomorphous to cementite. It is also stable in certain composition ranges, but generally appears as a transitional phase between the Fe_3C and M_6C carbides. The reaction sequence starts with the Fe_3C initially, then the Fe_2MoC forms, and finally the M_6C.

In 1962, Sato et al [14], removed carbides electrolytically from molybdenum steels that were austenitized at 1200°C and subsequently tempered at 700°C for 24 and 500 hours. More specimens were quenched after austenization at 900°C for 5 and 50 hours. Five types of stable carbides were found in the materials, Table 2.2.

Table 2.1: Atomic Ratios for Fe-Mo Carbides, Kuo [11]

Ratio (Mo:C)	Phase
< 1	MoC & Fe_3C
1	MoC
1 < ratio < 2-3	MoC & M_6C
2-3 < ratio < 4-5	M_6C
< 4-5	M_6C & Fe_7Mo_6

The authors constructed isothermal diagrams above and below the eutectoid, at 700°C and 900°C. They found the carbides that formed after 24 hours at 700°C had a different composition from those formed at 500 hours and in some instances were different carbides altogether. After 500 hours some alloys still had extra phases, with respect to equilibrium, which indicated that some of the reactions were still incomplete. This was attributed to the overall sluggishness of the molybdenum alloy steels.

The stable carbides after 24 hours at 700°C included M_3C, Fe_2MoC, and M_6C. The Mo_2C carbide was considered to be an intermediate phase. After 500 hours at 700°C, the same carbides were stable. The $M_{23}C_6$ carbide was confirmed to be metastable. The specimens quenched from 900°C revealed the same group of stable carbides after five hours at temperature. The Mo_2C carbide disappeared after 50 hours. The Mo_2C is a transitional phase in molybdenum steels, replaced by Fe_2MoC or M_6C after tempering, but, is known to be stable in the high carbon and molybdenum alloys. The carbide morphology is given in Table 2.3.

Table 2.2: Stable Fe-Mo Carbides (wt%), Sato et al [14]

Formula	Structure	Carbon	Molybdenum
M_3C	orthorhombic	6.67%	2%
$M_{23}C_6$	face centered cubic	5.0-6.0%	6-13%
Fe_2MoC	orthorhombic	5.5-6.0%	25-37%
M_6C	face centered cubic	2.5-2.8%	45-62%
Mo_2C	hexagonal	6.0%	70%

Fraker and Stadelmaier [15] arc melted sintered powders and annealed them at 1250°C for 20 hours and then again at 1000°C for 150 hours followed by a water quench. The compositional matrix of the specimens were between approximately 3 to 25 at% carbon and 20 to 80 at% molybdenum. They varied the composition of the alloys and paid particular attention to the partitioning of iron and molybdenum. As the composition changed from the iron-rich to the molybdenum-rich end of the alloy range the lattice parameters of the M_6C phase also changed, Table 2.4. This was also the only ternary phase identified.

Table 2.3: Fe-Mo Carbide Morphology, Sato et al [14]

Carbide	Description
M_3C & $M_{23}C_6$	Plate-like or dendritic.
Mo_2C	Stringy or rod-like.
M_6C	Globular.
Fe_2MoC	Not remarkable; May be a result of reactions: $M_{23}C_6 \rightarrow Fe_2MoC$ or $Mo_2C \rightarrow Fe_2MoC$.

The $M_{23}C_6$ carbide was not found and it was suggested that it decomposed during annealing. Contrary to Kuo's work, they did not find the Mo_4Fe_2C for which he reported a 1.126Å lattice parameter.

Table 2.4: M_6C Lattice Parameters, Fraker et al [15]

Lattice Parameter (Å)	**Composition** (at%)
1.1095	42% Mo 44% Fe 14% C
1.1122	43% Mo 43% Fe 14% C
1.1140	44% Mo 42% Fe 14% C

2.1.1 Fe-Mo Binary System

Rivlin's extensive review of the Fe-Mo-C system began with some of the earliest published work on the system. He also covered the Fe-Mo binary system in the same publication, Figure 2.1. The hexagonal intermetallic *R*-phase, Fe_5Mo_3, is 50 wt% molybdenum and forms peritectically at 1488°C. It decomposes eutectoidally at 1200°C to α-Fe and Fe_7Mo_6. Sinha et al [17] established the $Fe_{63}Mo_{37}$ structure for the *R*-phase in 1967. His X-ray diffraction and dilatometry work was performed on a 37.4 at% molybdenum alloy. The phase was described as having only high temperature stability although it required prolonged tempering to decompose entirely. The *R*-phase was discussed in the work of Komura et al [18] in 1959 and Heijwegen and Rieck [19] in 1974. Heijwegen and Rieck found that it formed only above 1200°C, but once formed, it was stable to room temperature and did not easily decompose.

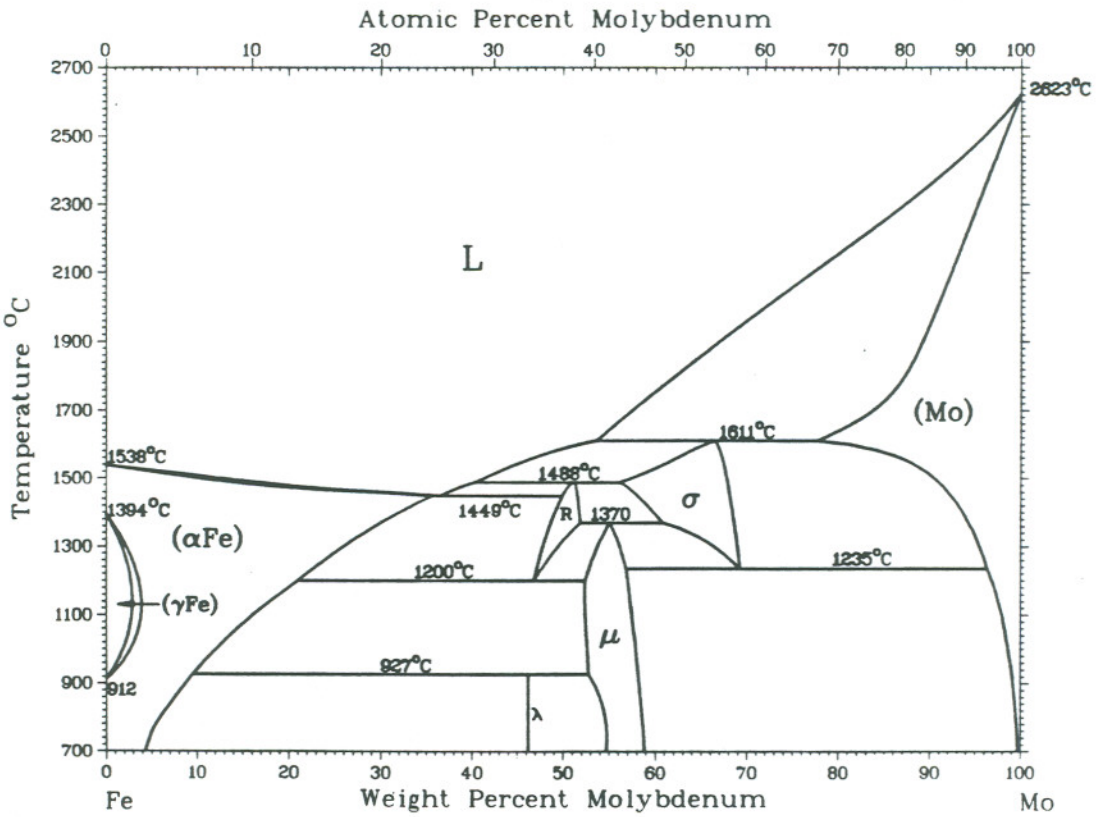

Figure 2.1 Binary phase diagram for the Fe - Mo system [16].

Sinha determined the Fe_7Mo_6 structure designation for the μ-phase which had previously been referred to as Fe_3Mo_2. The Fe_7Mo_6 forms peritectoidally at 1370°C at 55 wt% molybdenum and is stable to room temperature. There is also an Fe_2Mo Laves phase which forms at a 927°C peritectoid at approximately 47 wt% molybdenum, and is stable to room temperature as well. Sinha described all of the Fe-Mo intermetallics as related structures and considered them to be variations of the tetrahedral stacking. The α-Fe field is shown to have a minima at 30% Mo and Rivlin gave the maximum solid solubility of molybdenum in iron for the binary system and corresponding reactions as follows:

35.7 wt% Mo at 1449°C	Peritectic: $L + Fe_5Mo_3 \rightarrow \alpha\text{-Fe}$
21.0 wt% Mo at1200°C	Eutectoid: $Fe_5Mo_3 \rightarrow \alpha\text{-Fe} + Fe_7Mo_6$
9.7 wt% Mo at 927°C	Peritectoid: $\alpha\text{-Fe} + Fe_7Mo_6 \rightarrow Fe_2Mo$

2.1.2 Fe-Mo-C Ternary System

Takei provided a construction of the isothermal liquidus contours in the iron corner of the ternary diagram including up to 3.5 wt% carbon and 50 wt% molybdenum [9]. Rivlin mentioned unexplained inconsistencies in the location of certain reactions in Takei's work. However, Takei's construction of the phase relationships have only recently been challenged experimentally. The binary phase diagrams that Takei used for Mo-C and Fe-Mo are now outdated, but the basic features have not changed. Rivlin [9] reproduced a modified version of the liquidus Jellinghaus constructed in 1968 and the reaction sequence from this work, Table 2.5, which is still commonly used. The M_6C phase is shown forming from a peritectic at 1470°C and going through five reactions.

Nishizawa [20] held specimens at 1000°C for 100 hours to equilibrate alloys using a carburizing method. Among other phases, he found α-Fe, γ-Fe, Fe_3C, Mo_2C, M_6C, Fe_2MoC, and Fe_3Mo_2 which is assumed to be the Fe_7Mo_6 intermetallic. Nishizawa recognized that the

Table 2.5: Jellinghaus Solidification Sequence, Rivlin [9]

U_4: 1270°C

$L + R\text{-phase} \rightarrow \delta\text{-Fe} + M_6C$

U_3: 1210C°C

$L + \delta\text{-Fe} \rightarrow \gamma\text{-Fe} + M_6C$

U_2: 1150°C

$L + M_6C \rightarrow \gamma\text{-Fe} + Mo_2C$

U_1: 1120°C

$L + C \rightarrow Mo_2C + \xi$

E_1: 1085°C

$L \rightarrow \gamma\text{-Fe} + Mo_2C + \xi$

NOTE: U_i = Transitional, E_i = Eutectic

diffraction patterns for his ternary carbide were similar to that of Kuo's M_aC_b and Dyson and Andrew's Fe_2MoC. He also associated them with Takei's unknown carbide and denoted it as the xi-phase (ξ). Four three-phase combinations and four two-phase combinations were identified by Nishizawa using microprobe analysis:

α-Fe + γ-Fe + M_6C	γ-Fe + Mo_2C
γ-Fe + Fe_2MoC + Mo_2C	γ-Fe + M_3C
γ-Fe + M_6C + Mo_2C	γ-Fe + M_6C
γ-Fe + Fe_2MoC + M_3C	γ-Fe + Fe_2MoC

Wada's liquidus surface [23], Figure 2.2, shows a eutectic reaction with $L \rightarrow M_3C + C + \gamma\text{-Fe}$. Jellinghaus showed the eutectic $L \rightarrow M_3C + Mo_2C + \gamma\text{-Fe}$ in an equilibrium version and the additional reaction $L + C \rightarrow M_3C + Mo_2C$ in a metastable version. Wada and Jellinghaus both show very similar M_6C phase fields.

In 1988, Andersson [21] performed a thermodynamic evaluation of the Fe-Mo-C system and provided a new Fe-Mo binary phase diagram. The phases and their structures were not disputed, however, the reaction temperatures were shifted approximately 10°C higher. Several calculated four-phase equilibria were listed and an Fe_2MoC phase field was provided on his liquidus surface, Figure 2.3. He also accepted the work of others who claimed this carbide to be stable to room temperature. Andersson disputed some of Rivlin's conclusions saying that they were thermodynamically inconsistent in linking various authors' work. The work of Campbell et al [13] was discredited based on the alloys allegedly being contaminated with unacceptably high levels of manganese and silicon. Sato had published lower molybdenum contents for his M_6C and Mo_2C carbides and Andersson claimed that some iron rich matrix material must have remained on Sato's isolated carbides.

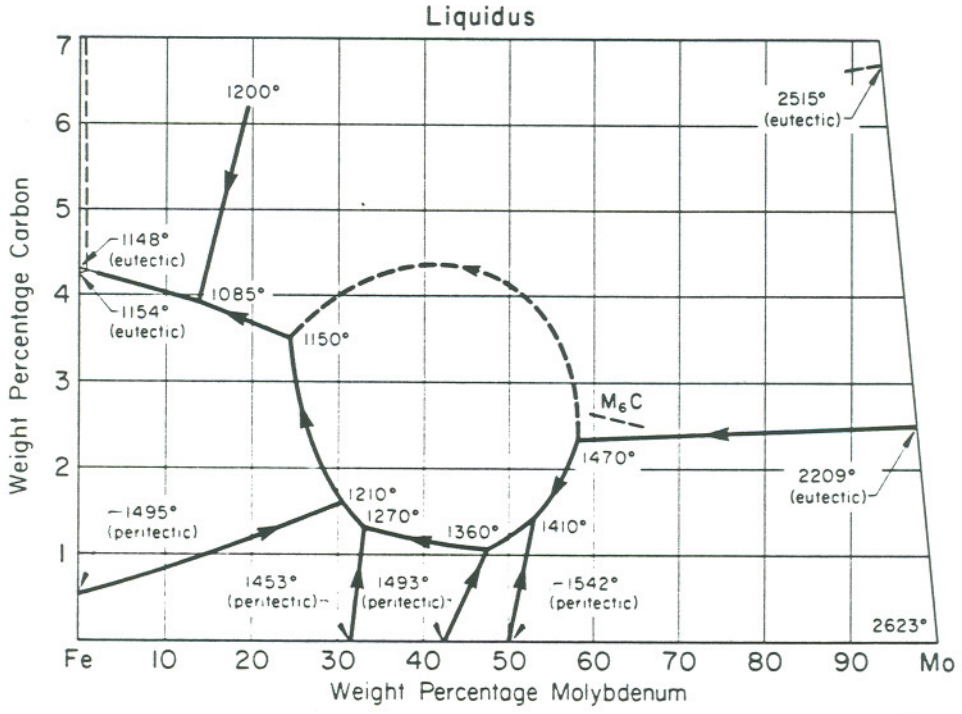

Figure 2.2 Wada's Liquidus surface for the Fe - Mo - C system [23].

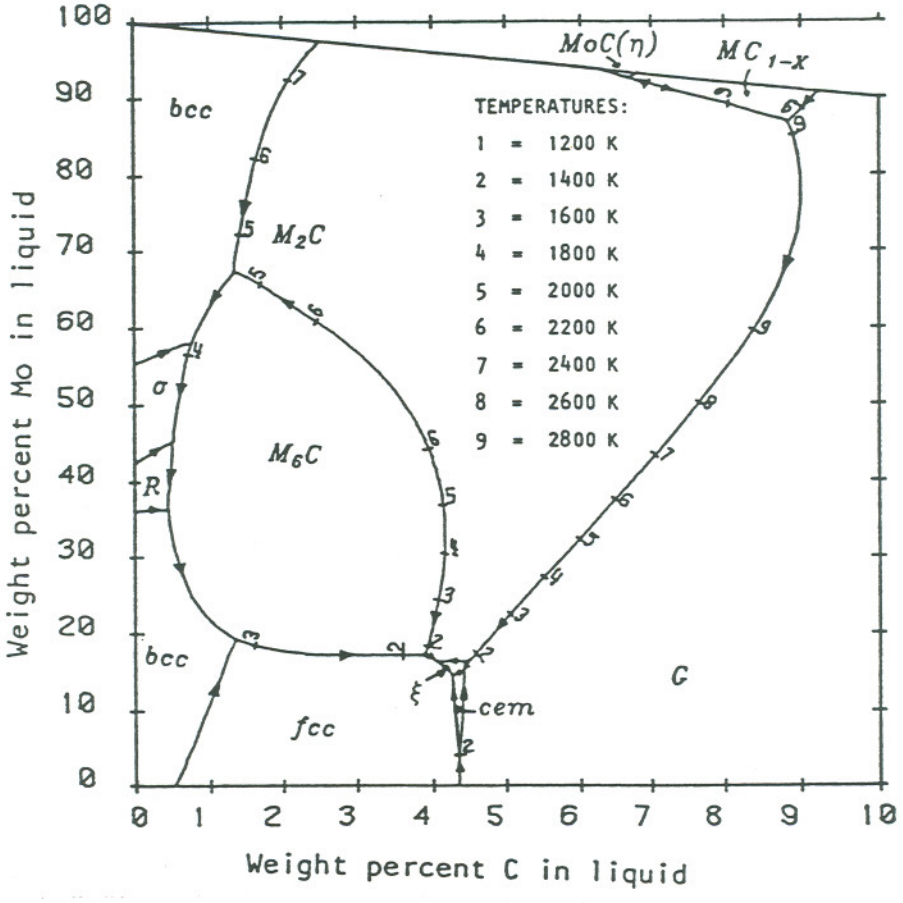

Figure 2.3 Andersson's liquidus surface for the Fe - Mo - C system [21].

Andersson's liquidus surface is very similar to that of Jellinghaus except for a more expansive M_6C phase field. It extended to lower carbon and molybdenum levels giving much narrower *R*-phase and FeMo phase fields. The liquidus valley separating the M_6C and Mo_2C carbide phase fields is less convoluted. The diagram also shows a narrower Fe C_3 phase field and a primary Fe_2MoC phase field.

Schuster et al [22] were looking for the solubility of iron in the Mo_2C carbide and found α-Fe instead of γ-Fe in conjunction with the carbide at 1000°C. This was not in accord with existing phase diagrams. This caused them to pursue a detailed examination of the Fe-Mo-C system. Their analytical tools included differential thermal analysis, melting point determination, X-Ray, and metallography on annealed specimens. They reported on the work of Wayne and Nowotny who isolated a single crystal of the ξ-carbide and determined the composition to be $Fe_{11}Mo_6C_5$ with a monoclinic structure. This also fitted with their thermodynamic calculations.

Schuster found a new primary crystallization field for the ξ-carbide in an area of the liquidus surface, Figure 2.4. His reactions are given in Table 2.6. Rivlin had concluded that the ξ-phase did not form from the liquid, but instead, from a ternary peritectoid, γ-Fe + Fe_3C + $Mo_2C \rightarrow \xi$. Andersson had proposed a ternary peritectic at 1086°C, L + C + $Mo_2C \rightarrow \xi$, with which Schuster did not agree and placed his peritectic, L + γ-Fe + $Mo_2C \rightarrow \xi$, at 1202°C. Schuster claimed the ξ-carbide to be unstable and did not show the phase to exist below 800°C. The existence of the ξ-carbide at 700°C had been controversial [11,13,10,14,19]. Wada's 1000°C and 700°C isotherms are shown in Figures 2.5 and 2.6.

Schuster [22] and Wada [23] both used the Fe_3Mo_2 structure designation for the intermediate intermetallic, Fe_7Mo_6. They were apparently not aware of some of the earlier literature [9,17,21] establishing this formula of the peritectoid phase. Schuster also lists an $FeMo_2$ intermetallic which is surely a typographical error. All other publications dealing with the Fe-Mo system discuss an Fe_2Mo Laves intermetallic. Hereafter, for the purposes of this document, the primary peritectic Fe_5Mo_3 or $Fe_{63}Mo_{37}$ and the secondary peritectoid Fe_3Mo_2 or Fe_7Mo_6 intermetallics will be referred to as the *R*-phase and *μ*-phase respectively. The Fe_2MoC ternary carbide will be referred to as the ξ-phase.

Table 2.6: Schuster's Solidification Sequence [22]

U_5: 1370°C

$L + R\text{-phase} \rightarrow \alpha\text{-Fe} + M_6C$

U_4: 1340°C

$L + \alpha\text{-Fe} \rightarrow \gamma\text{-Fe} + M_6C$

U_3: 1300°C

$L + M_6C \rightarrow \gamma\text{-Fe} + Mo_2C$

P_1: 1202°C

$L + \gamma\text{-Fe} + Mo_2C \rightarrow \xi$

U_1: 1183°C

$L + Mo_2C \rightarrow Fe_3C + \xi$

or

E_1: 1123°C

$L \rightarrow \gamma\text{-Fe} + Fe_3C + \xi$

NOTE: U_i = Transitional, P_i = Peritectic, E_i = Eutectic

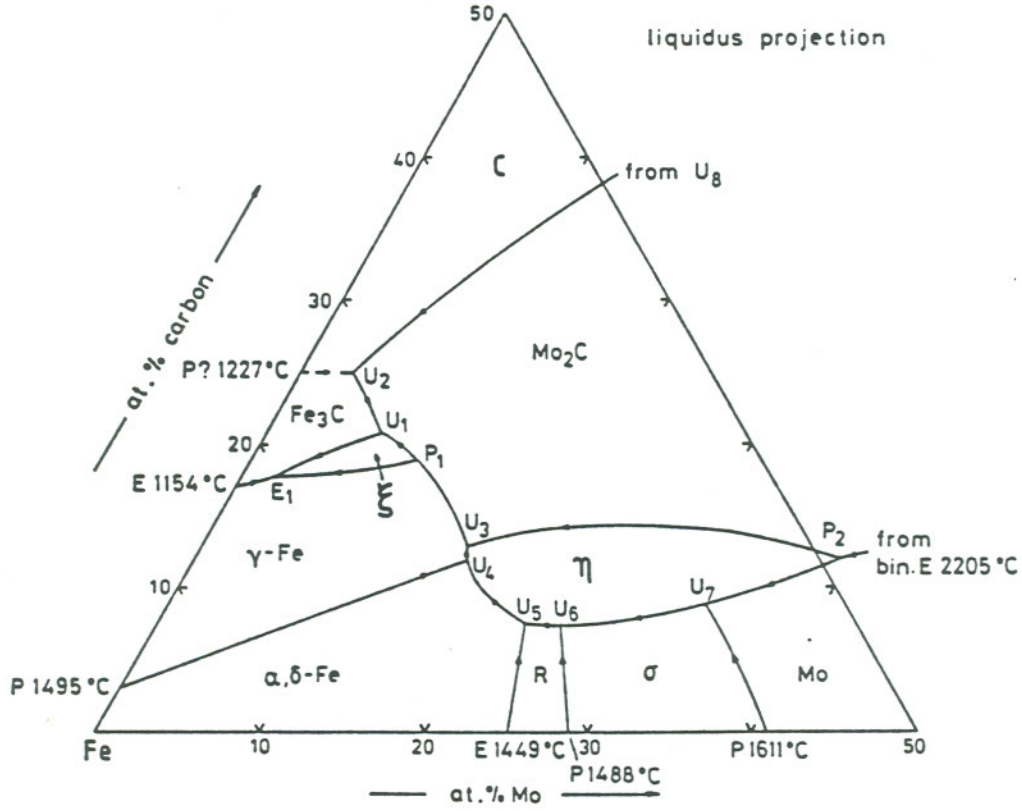

Figure 2.4 Schuster's liquidus surface for the Fe - Mo - C system [22].

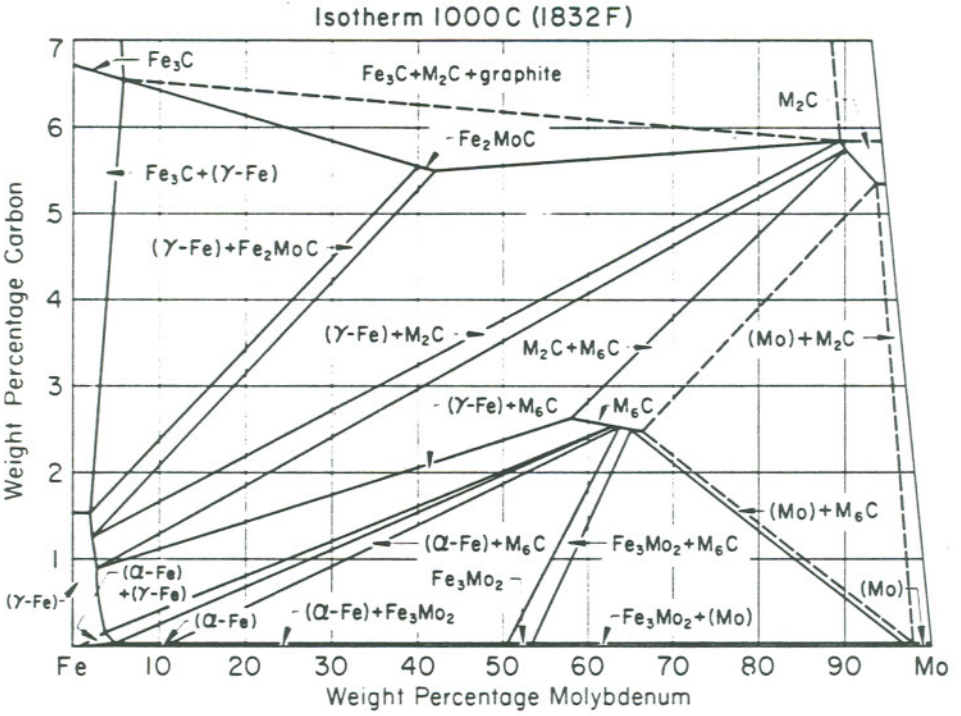

Figure 2.5 1000°C isotherm for the Fe - Mo - C system [23].

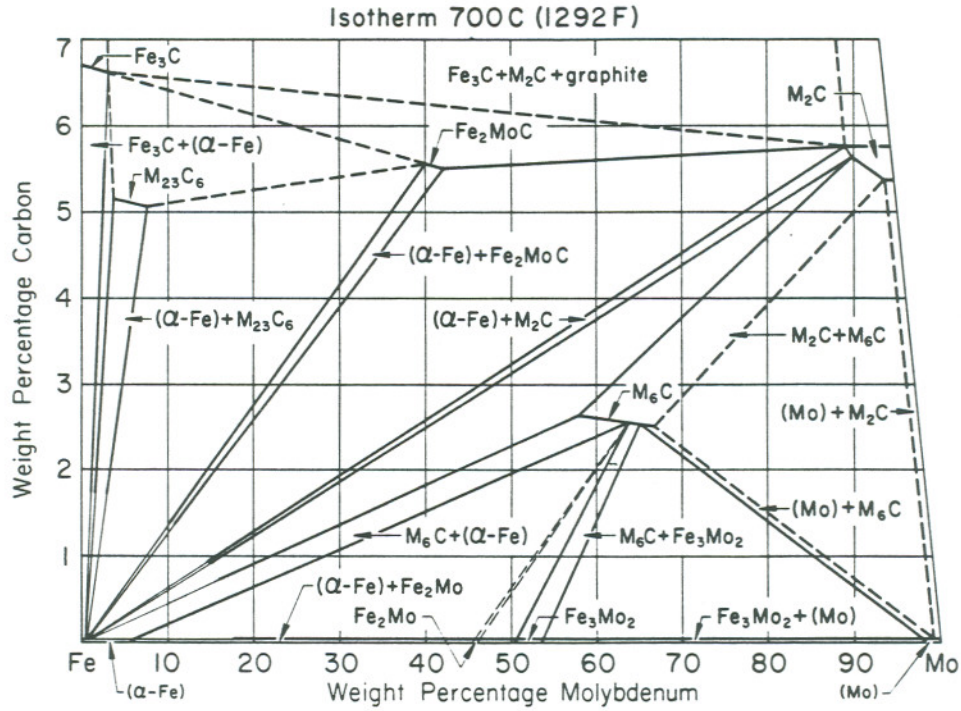

Figure 2.6 700°C isotherm for the Fe - Mo - C system [23].

2.1.3 The Hardness of Carbides

Leckie-Ewing [24] took hardness readings of carbides in an M1 tool which contained 8.5% Mo. The alloy was quenched and tempered to HR_C 65 and contained MC and M_6C carbides. The majority of the carbides found were the M_6C type consisting of primarily Fe_4W_2C and some Fe_4Mo_2C which Kuo had found. The M_6C carbides containing molybdenum were reported to be in the same hardness range as that of the chromium carbides, Table 1.1.

Leckie-Ewing used a 4% aqueous solution of NaOH saturated with potassium permanganate ($KMnO_4$) and a 1% solution of chromic acid etched electrolytically at 3 volts for 3 to 5 seconds to identify the carbides for his study. The M_6C stained brown in the NaOH/potassium permanganate solution.

2.2 Abrasive Wear

2.2.1 Definition

Wear, as defined by the Organization for Economic Cooperation and Development (OECD) [25], is "The progressive loss of substance from the operating surfaces of a body occurring as a result of relative motion at the surface." This general description includes wear as a result of particles trapped between the surfaces, embedded particles in one surface running against another surface, or particles rolling and/or sliding over a surface. These are examples of abrasive wear.

2.2.2 Description

An abrasive wear condition is often described as a two-body or three-body system. The two-body abrasive wear system consists of a rough surface moving relative to another surface while they are in contact and under a load. Individual abrasive particles or asperities are held rigid relative to the abraded surface. The three-body abrasive wear system consists of two surfaces moving relative to one another under a load with a third body, the abrasive,

trapped in between. The abrasive in this case is free to move relative to the surfaces in motion and with respect to other abrasives.

From observations of worn surfaces, Blickensderfer [26] found that two-body abrasion tended to produce plowing and cutting of the surface by the abrasive material. The three-body abrasion tended to produce deformation in the component surfaces. These are often referred to as high stress or low stress conditions, respectively. The high stress condition occurs in the two-body system as a result of the abrasive being held in place and supported in a rigid fashion. The low stress condition, as found in a three-body system, is the result of the abrasives ability to move and roll and reduce the stress intensity. Blickensderfer points out, however, that the high and low stress terms do not define a wear condition, but relate to whether or not the abrasive is primarily being crushed during the wear process.

Avery [27] define these terms as follows:

High Stress Abrasion -

Fragmentation of abrasive, work hardening, and impact loading.

Low Stress Abrasion -

No work hardening, particles do not fracture, and no impact.

Abrasive wear has been categorized using a variety of different terms but often with similar definitions. Avery [28] defined two general categories of abrasive wear that relate to the level of impact, the physical changes in the abraded surface, and the break-down of the abrasive:

Gouging -

Impact loading, usually grinding or high stress abrasion, cutting and deformation, fragmentation of abrasive, strain hardening of surface, and particles are broken down.

Scratching -

Low stress abrasion, relatively light rubbing, low material removal, no appreciable work hardening, particles do not fracture.

2.3 Models

2.3.1 Moore

One of the first attempts at developing a simple abrasive wear model was developed by Moore [29]. The model was based on an irregular abrasive particle that penetrates a surface and slides parallel to it under a normal load. The equation gives wear in volume per unit area, V, using sliding distance, L, hardness, H, and the load per unit area, σ.

$$V = \frac{k \cdot K \cdot C \cdot L \cdot \sigma}{H}$$

The constants k, K, and C, provide an abrasive particle shape factor, the number of abrasives in contact and causing material to be removed, and a proportionality constant for the amount of the groove volume removed as wear debris. This equation is independent of particle size. Particle shape, critical attack angle, and depth of penetration are accommodated through the proportionality constants.

2.3.2 Archard

Archard's model [30] is based on an inverted right cone with a normal load, N, sliding parallel to a surface where the point of the cone can penetrate the surface. The hardness is given as load over a projected area where the area term relates to the frontal area of the cone that has penetrated the surface. This also accounts for the depth of penetration and conversely, the volume of the groove.

The volume loss, V, over sliding distance, L, is given as:

$$V = \frac{K \cdot 2 \cdot \cot\alpha \cdot N}{\pi \cdot H}$$

where the trigonometric term relates to the groove volume and accounts for particle size and depth of penetration. The constant, K, gives the portion of asperity contacts making grooves. The K - constant has been estimated to be $5x10^{-3}$ for three-body wear and $5x10^{-2}$ for two-body wear.

2.3.3 Rabinowicz

The Rabinowicz [31] model will be considered in greater detail. Rabinowicz developed a model regarding a single hard asperity in the form of an inverted cone under a normal load, P, Figure 2.7. The load is sufficient to cause the asperity to penetrate the surface to a given depth. Therefore, the load is directly related to the cross-sectional area of the cone at the surface, and by definition, the hardness of the surface material, H. The radius, r, of the cone is taken at the surface.

$$P = A \cdot H = \pi \cdot r^2 \cdot H \qquad \text{Eqn 1}$$

Rabinowicz calculated the groove volume, V, as a function of the cross-sectional area of the asperity in the vertical plane, again using the radius, r, and the depth of penetration, h. The cone sweeps out volume δV in distance δl.

$$\delta V = r \cdot h \cdot \delta l \qquad \text{Eqn 2}$$

The angle, θ, between the leading edge of the asperity and the abraded surface is described by Equation 3.

$$h = r \cdot \tan\theta \qquad \text{Eqn 3}$$

This can be substituted into Equation 2, as shown in Equation 4. Then solving Equation 1 for r^2, substituting into Equation 4, and integrating, gives Equation 5.

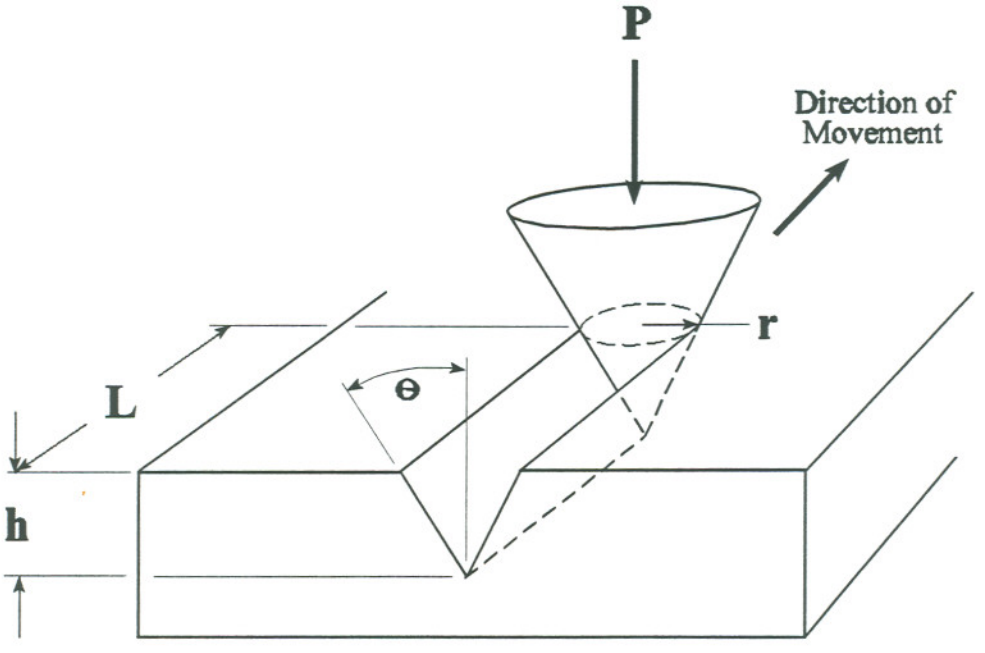

Figure 2.7 An illustration of Rabinowicz model.

$$\delta V = r^2 \cdot \tan\theta \cdot \delta l \qquad \text{Eqn 4}$$

$$V = \frac{P \cdot \tan\theta \cdot l}{\pi} \cdot H \qquad \text{Eqn 5}$$

Considering multiple asperities, a weighted average can be taken for tan θ. Further assumptions include this and the percentage of the groove removed, the percentage of contacting particles, their shape, orientation and dispersion, and the number of particles in contact through a constant, *K*, giving equation 6. For three-body wear, the *K*-value ranges between $2 \cdot 10^{-3}$ and $6 \cdot 10^{-3}$.

$$V = \frac{K \cdot P \cdot l \cdot \tan\theta}{\pi} \cdot H \qquad \text{Eqn 6}$$

The models described here are all linearly dependent on load, sliding distance, and are proportional to particle shape and depth of penetration at least indirectly. They are only capable of predicting linear volume loss, assuming all of the constants were known for a given material. At best; they could be used to determine an approximation of applied load versus wear rate for a given wear system.

2.3 Influences on Abrasive Wear

The characteristics of abrasive wear depend on a multitude of variables for both the abrasive and the abraded materials. There is an abundance of literature available describing every imaginable combination and a wide variety of test methods. Two of the most common abrasive wear tests are the Pin-on-Disk test for a two-body abrasion system, and the Dry Sand Rubber Wheel test for a three-body abrasion system.

The Pin-on-Disk machine consists of a pin specimen that is loaded against a rotating cylinder, or disk, covered with abrasive paper. The pin is translated across the abrasive surface during the test such that it is always in contact with fresh abrasive. With the Dry Sand Rubber Wheel machine, the abrasive particles are fed at a constant rate between a rubber wheel and the test specimen, which is pressed against the wheel at a constant load. Both tests can be run continuously, or, for a set number of revolutions, or distance traveled. When the rotating component is periodically stopped, the specimen can be removed from the machine and weighed. The weight, or mass, loss of the specimen is plotted against the number of revolutions or sliding distance for each interval. This sequence is repeated several times until a constant wear rate is achieved. The wear rate is calculated from a regression of the slope of the linear portion of the weight loss versus sliding distance line.

Misra and Finnie [32] looked at the variables affecting two-body and three-body abrasion on pure metals. The parameters examined were material hardness, work hardening, applied load, distance traveled, abrasive particle size, and the abrasive hardness. They concluded that the effects were the same for both wear types but that the difference in wear was greater than one order of magnitude for the two-body Pin-on-Disk test.

Rabinowicz [31] states that there is no difference in geometry between two and three body wear systems. Therefore, the difference has to be abrasive particle rolling in three body wear. He estimates that rolling occurs approximately 90% of the time and points to low friction coefficients measured in three body systems as evidence.

2.4.1 Effect of Matrix Phase

Fiore et al [35] looked at the effect on wear behavior of varying amounts of austenite in the matrix of some Ni-Hard-IV alloys. The materials were produced with austenite volume fractions of 5, 20, 40, and 85%, with hardness of 64, 63, 61, and 47 HR_C. Wear tests were performed using silica and alumina in a Dry Sand Rubber Wheel test and bonded alumina in a Block on Ring test. The data are compared with Pin-on-Disk data with garnet and alumina from Climax Molybdenum Laboratories. The Dry Sand Rubber Wheel test was defined as low stress abrasion; the block on ring test as gouging, or high stress abrasion.

The Pin-on-Disk test and the Dry Sand Rubber Wheel test with the softer abrasives produced a maximum weight loss at a specimen hardness which correlated with approximately 40% retained austenite. The Block on Ring tests using alumina abrasives showed a minimum at approximately the same level. The Dry Sand Rubber Wheel test with alumina showed much different behavior with monotonically increasing wear with increasing hardness. The weight losses produced by the harder and more angular alumina abrasive in these tests was significantly greater. Under no conditions with any of the tests did the wear rates decrease with increasing hardness.

No single wear mechanism could explain the variations in weight loss shown with the various testing devices. There was some evidence of fracture in the carbides in the specimens which experienced the greatest weight loss, however, the major differences were related to the work hardenability and impact resistance of the retained austenite. The mechanism was primarily a result of micromachining in both the matrix and the carbides.

Fiore also discussed work by Zum Gahr with low alloy tool steels heat treated to varying levels of retained austenite. The materials were tested using a pin-on-disk test with alumina. The weight loss data showed a minimum at intermediate retained austenite contents which was opposite from the findings of Fiore et al. It was postulated that stress induced martensite generated compressive residual stresses in the surfaces of Zum Gahr's materials which retarded the formation of cracks in the matrix. This also provided a material with greater strength on the surface and a tougher more ductile material below the surface.

Zum Gahr [34] studied the abrasion resistance as a function of matrix phase in a series of white irons with carbide volume fraction ranging from 7% to 39%. Two sets of alloys were developed with matrix phases of predominately austenite or martensite. Dry Sand Rubber Wheel tests were carried out using silica sand as the abrasive. Both the austenitic and martensitic materials experienced a minimum wear rate at approximately 30% carbide volume fraction. The austenitic alloys experienced a slightly higher wear rate.

Gundlach and Parks [5] performed Pin-on-Disk testing using alumina, garnet, and silicon carbide abrasives. They found retained austenite superior to martensite for the harder

alumina and silicon carbide abrasives. The martensitic matrix was found to be equal to, or better than the austenite with the softer garnet abrasive. A martensitic matrix showed superior performance in Zum Gahr's [34] Wet Sand Rubber Wheel test and pin test with garnet abrasive. The austenitic material had a lower wear rate with the harder silica abrasive which was attributed to the greater work hardenability and ductility of the phase.

2.4.2 Effect of Carbide Volume Fraction

Fulcher et al [33] performed Dry Sand Rubber Wheel testing on a series of high chromium white irons obtained from Zum Gahr. Carbide volume fractions for these alloys ranged from 9% to 39%. The abrasive material was 200 to 300 μm quartz sand. A minimum wear rate was found at the eutectic composition. Quartz sand tests on a hypoeutectic material showed increasing wear resistance with increasing carbide volume fraction. As the eutectic composition was approached, more and more matrix material was protected due to the close spacing of the eutectic carbide particles. The wear rate increased in the hypereutectic composition range when the massive carbides protruded above the matrix and became unsupported and vulnerable to fracture, Figure 2.8.

These results were supported by Zum-Gahr who [34] performed Wet Sand Rubber Wheel tests and pin-on-drum tests on the same series of chromium irons. The Wet Sand Rubber Wheel test was run with 200 to 300μm quartz sand. The pin test was run with both 100μm garnet and 80μm SiC. The carbide volume fraction for the microstructures ranged from 7% to 45%.

The results showed a minimum wear rate for the quartz Wet Sand Rubber Wheel test at approximately 30% carbide volume fraction. The increasing wear was attributed to the spalling of the massive carbides that were present in the materials having greater than 30% carbide volume fraction. The garnet was far softer than the carbides, which enabled the carbides to protect the matrix material. The silica was able to penetrate the carbides thus producing the greater wear loss at higher carbide volume fraction.

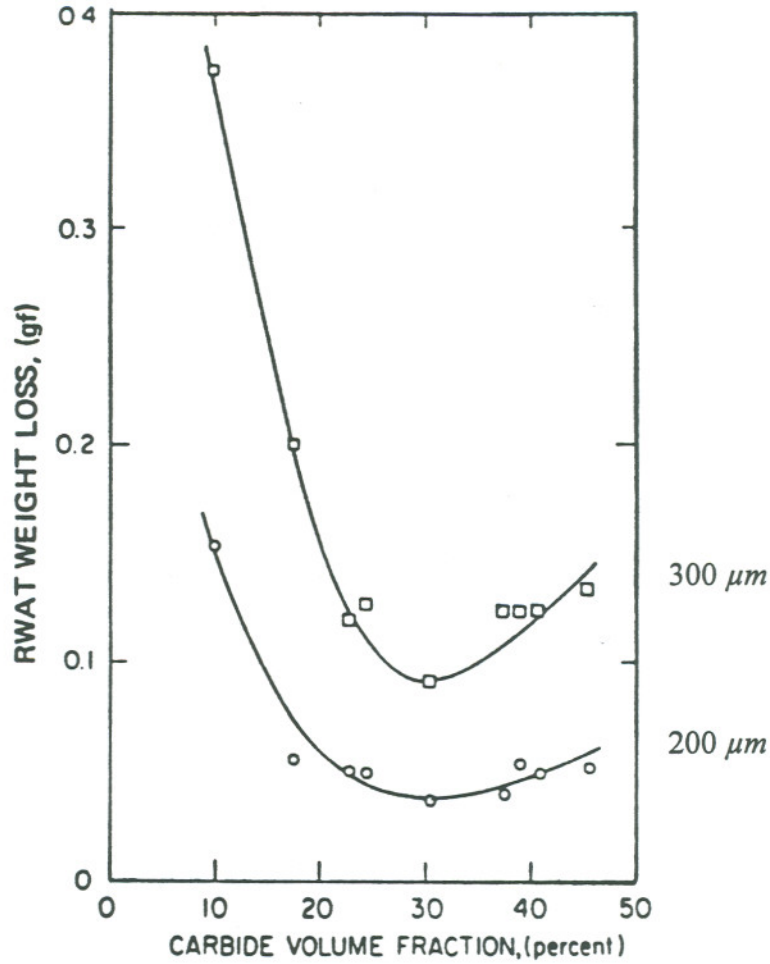

Figure 2.8 Fulcher's Dry Sand Rubber Wheel data for 200 and 300 μm diameter silica [33].

2.4.3 Effect of Carbide Size

The effect of carbide size was examined by Desai et al [39], who produced several cobalt-based alloys with varying carbide size and with constant carbide volume fraction. They performed Dry Sand Rubber Wheel tests with alumina and silica. Very small carbides, found in the highest and lowest carbide volume fraction alloys, were removed with the chips formed during the abrasion process. This caused the wear rates at the high and low carbide volume fraction levels to be greater and created a parabolic curve, Figure 2.9, or what Desai called the reversal of the wear curve. The larger carbides tended to protrude above the matrix when silica abrasive was used because the abrasives could not cut the harder carbides. To a limited extent, the alumina abrasive would leave the carbides in relief where micromachining was the predominant material removal mechanism. Earlier work by this group implied that there was a maximum wear resistance associated with carbide size relative to the abrasive size. The present work suggested that size was also a major factor in the wear behavior.

Kulik and Kosel [40] found that there was a direct correlation between the total edge length of second phase particles and wear for model alloys. The alloys were prepared from sintered copper powder with alumina or tungsten carbide hard phase particles sieved to separate them for size. Tests were performed using a pin-on-disk machine with garnet, alumina, and silicon carbide abrasives. The abrasion rate was established as a function of the second phase particle size. The wear rate showed a linear relationship with the sum of the edge lengths of the second phase particles. Their hypothesis was that larger lengths of exposed edges provided a greater amount of unsupported edge that could potentially fracture.

Silence [37] performed Dry Sand Rubber Wheel tests on cast two-phase materials. The materials consisted of irons cast in sand and graphite molds. A distinctly finer structure was obtained with the graphite mold cast materials. The carbides were typically in the range of 2 - 10 μm in diameter for the entire group of alloys. Greater wear, by a factor of 2.5 to 10 times, was found with the finer structure even when the coarser sand molded materials were several Rockwell hardness points softer.

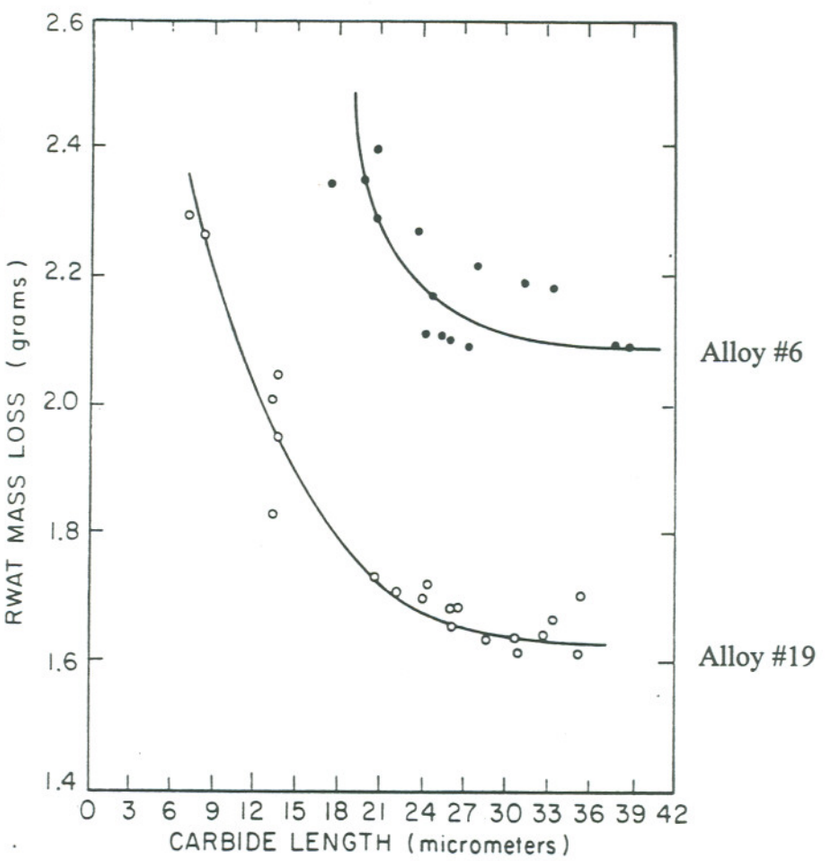

Figure 2.9 Weight loss versus carbide length [39].

2.4.4 Effect of Abrasive Size

Kosel et al [41] looked at the effect of abrasive size on a 1020 steel and Stellite alloy #19 with Dry Sand Rubber Wheel testing using alumina and quartz. They found a monotonically increasing wear rate with increasing abrasive size for the steel with alumina and quartz, and Stellite with alumina. A decreasing wear rate was found for the Stellite with increasing quartz abrasive size. The weight loss of Stellite by the quartz abrasive was dependent on fracture occurring at the carbide edges. However, at higher carbide volume

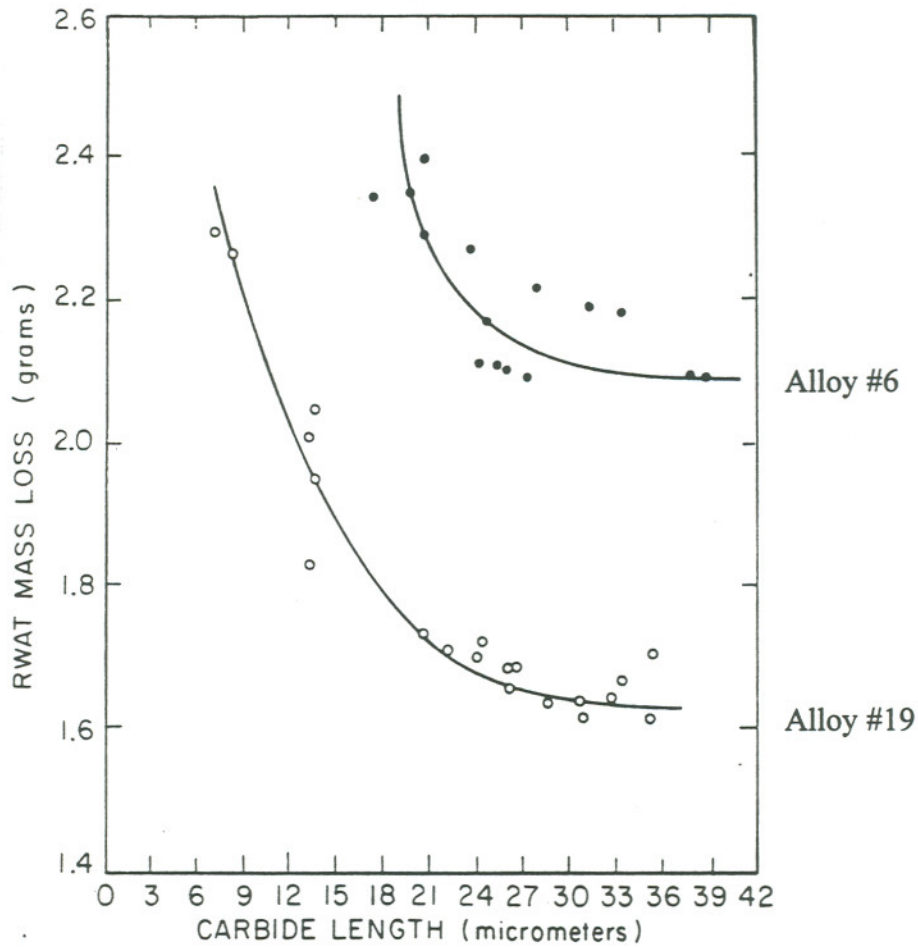

Figure 2.9 Weight loss versus carbide length [39].

2.4.4 Effect of Abrasive Size

Kosel et al [41] looked at the effect of abrasive size on a 1020 steel and Stellite alloy #19 with Dry Sand Rubber Wheel testing using alumina and quartz. They found a monotonically increasing wear rate with increasing abrasive size for the steel with alumina and quartz, and Stellite with alumina. A decreasing wear rate was found for the Stellite with increasing quartz abrasive size. The weight loss of Stellite by the quartz abrasive was dependent on fracture occurring at the carbide edges. However, at higher carbide volume fraction, the larger quartz abrasive could not penetrate between the carbides. Using the alumina abrasive, the Stellite alloy did not follow this trend. Instead, a micromachining mechanism was found with the harder alumina cutting through the carbides.

The abrasive size effects were also tested by Kulik and Kosel [40] on their model alloys. They showed a significant increase in wear rate with a larger abrasive size. Their examination of wear surfaces showed a greater frequency of fracture in the hard phase with larger abrasive size.

Huard et al [42] looked at the effect of particle size and shape on Dry Sand Rubber Wheel wear rates on 1020 steels. They analyzed the sand size and shape quantitatively using image analysis techniques. The testing was carried out using two different sands described as an Ottawa standard 200 - 300 μm diameter sand and a non-standard rounded 200 - 300 μm foundry sand. The Ottawa sand was much more angular, and after sieving, the foundry sand was found to have a greater percentage of larger particles.

Huard found a decreasing wear rate with increasing grit size when plotted against the mean diameter of the abrasive as measured by image analysis methods. The spherical abrasive increased wear to a point and then quickly experienced diminishing returns. The abrasive particles needed to be very large before size no longer had an influence. Non-spherical abrasive increased wear with increasing size, however, angular abrasives also increased in roundness with increasing size resulting in a decreasing wear rate. The smaller grit tended to have a higher angularity and was less likely to roll providing a more efficient wearing action.

In the work of Kosel et al [41], the smaller abrasive was thought to penetrate between the carbides to produce a greater wear rate. This is in opposition to the findings of other workers. Kosel's work was questioned by Huard, as the angularity of the grit was not measured. Test results on 1020 steel were more conventional, showing increasing wear with increasing grit size.

Misra and Finnie [43] reviewed the literature to examine the theories relating to why abrasive particles below 100 μm became less efficient in two and three body abrasive wear and erosion. They concluded that all but one theory could be discounted by assuming that the abrasion and erosion wear types shared similar mechanisms and making direct comparisons between the wear types to determine if the theories fit both situations. It was postulated that the particle size determined the depth of the hardened surface layers and alternatively the strength of the material at the surface. The layers were significantly harder than the bulk material. They found that the sub-100 μm particles could not generate a work hardened layer to the extent that the larger particles could.

2.4.5 Effect of Hardness

Gundlach and Parks [5] used three different abrasives of varying hardness in pin-on-drum testing. A greater separation in wear resistance was found between the various white irons and steels tested with a softer garnet abrasive. This is similar to the results of Leech [38] who used a pin-on-drum test with 120 μm garnet and 80 μm alumina abrasive cloth on hardfacing alloys. Leech found the pin test with garnet to have greater sensitivity to various microstructures than the Dry Sand Rubber Wheel test.

Kulik and Kosel [40] demonstrated that the wear behavior of two phase materials was dependent on the abrasive particle hardness. They showed decreasing wear for silicon carbide, alumina, and garnet respectively. Austenitic white irons did better with abrasives that were as hard or harder than the carbides. When the abrasives were softer than the carbides, the martensitic irons did better.

Fulcher's Dry Sand Rubber Wheel investigation of chromium white irons also included testing with 200 - 300 μm alumina and quartz. The results were found to be dependent on the type of abrasive. The harder alumina particles produced a continuous decrease in wear rate with increasing carbide volume fraction. This was quite different from the quartz material results which showed a decrease in wear resistance when massive primary carbides were present in the microstructure The quartz abrasive ultimately caused the large carbides to fracture, producing an increase in wear. The alumina was found to cut through both soft and hard phases such that carbide fracture did not occur in any case.

Leech [38] used a pin-on-drum test with 120 μm garnet and 80 μm alumina abrasive cloth on hardfacing alloys. He based his work on that of Watson and Mutton who looked at the relationship of the hardness of the metal, (H_m) the abrasive, (H_a) and carbide, (H_c) on wear resistance. Watson found large increases in wear resistance for $H_m/H_a > 0.5$-0.6 and $H_c/H_a > 0.8$. Leech found that the phenomenon of increasing wear resistance with respect to hardness is actually a combined result of carbide volume fraction, matrix hardness, and decreased mean free path between the hard phases. The affect of matrix hardness was also greater with softer abrasives.

2.4.6 Dry Sand Rubber Wheel Testing

Several authors related their experiences with the idiosyncrasies of the Dry Sand Rubber Wheel test. Huard [42] found an 8% decrease in wear rate when the rubber wheel was brushed to remove embedded sand. The authors felt that the larger particles of sand tended to become embedded in the wheel because they accepted a greater portion of the applied load, as a result of their height. The smaller particles had more freedom to roll, or, the larger particles created greater damage due to sliding. They also found rounding of the grit and a general breakdown of the abrasive giving a greater number of smaller abrasive particles after a test. The sand did not always embed in the wheel and this was accredited to either the humidity, condition of the rubber wheel, or the abrasive shape. It was also hypothesized that an abrasive particle could be pushed into the rubber wheel during the

course of a Dry Sand Rubber Wheel test thereby causing a decrease in the depth of cut. This effect was not observed with the higher stress pin tests.

Kosel et al [41] found some difficulty maintaining a constant flow rate of sand during the Dry Sand Rubber Wheel tests. Some tests were run to determine the effect of a variable flow rate. The results showed that there was only a weak correlation between wear rate and the flow rate of the sand. The indications were that the sand curtain falling in between the wheel and the specimen were relatively uniform and that there was a certain amount of overflow to the sides of the contact area.

CHAPTER 3.
EXPERIMENTAL PROCEDURES

3.1 Measurement of Alloy Chemistries

Carbon contents were measured using a Leco Model CS 46 Carbon-Sulfur Combustion Analyzer. The molybdenum content for the experimental alloys was high enough that they were out of the calibration matrix for this instrument. There was also a concern about the ability of the instrument to reach the temperatures necessary to properly burn the high molybdenum samples. This left some doubt about the accuracy of the measured carbon levels. However, this was not considered to be a major concern as the carbide volume fraction (CVF) contained in the steels was not great enough to be meaningful in the wear data. Further, the relative percent error for the high carbon irons was even less significant. The molybdenum contents were measured using a Kevex Energy Dispersive X-Ray (EDX) device in combination with a AMR Model 1200 Scanning Electron Microscope (SEM). The capability of the Kevex to quantitatively measure the molybdenum content of the samples was checked using a Bureau of Standards certified sample. As the unit was not capable of measuring light elements, the previously measured percent carbon values were manually entered into the Kevex computer.

3.2 Specimen Preparation

3.2.1 Molybdenum Alloys

Experimental alloy compositions were selected with two criteria in mind. First, to generate samples with compositions characteristic of the various phase fields found on the liquidus surface, and second, to yield microstructures containing hard phases that might

display interesting abrasive wear results. The samples were produced using powder metallurgy techniques as described below. Nominal additions of alloy blended for melting are recorded in Table 3.1. All alloy compositions are represented as weight percent (wt%).

For each alloy, powders were weighed and placed in 250 *ml* plastic bottles along with four 15 *mm* stainless steel mixing balls. A rack of several bottles were then rotated in a ball mill for approximately 12 hours. The dry blend was mixed with a binder which consisted of a saturated solution of heptane and wax. The excess binder was decanted off and the mixture was dried at 115°C in a furnace under vacuum for 2 hours.

Table 3.1: Nominal Alloy Additions for Melting

Identification	C%	Mo%	Fe%
Alloy #2	0.5	25	balance
Alloy #3	0.7	25	-
Alloy #4	0.7	35	-
Alloy #5	2.0	20	-
Alloy #6	3.0	20	-
Alloy #7	3.0	30	-
Alloy #8	4.5	30	-

The alloy mixtures were then pressed into 12 x 15 x 75 *mm* bars at a pressure of 125 MPa with a 30 ton capacity hydraulic press. The die was filled level full with the alloy powder before pressing. Dewaxing was performed at 425°C for 3 hours under vacuum in a furnace fitted with a cooled trap to collect the wax that emerged from the green bars. Because they were very delicate, and to minimize handling between furnaces, dewaxing was performed on graphite trays that were also used for sintering.

The bars were sintered in a resistively heated, molybdenum lined, Brew vacuum furnace at a temperature of 1000°C for 4 hours at a vacuum level of 4 μm. The green bars on the graphite trays were stacked in a cylindrical graphite can with a side hole. The assembly was aligned such that a portion of one alloy bar could be seen through the hole.

The hole was then aligned with a glass sight in the door of the furnace, opposite an optical pyrometer. The furnace was manually controlled while the temperature was monitored with the pyrometer.

The sintered bars were melted into solid bars using an arc melt furnace with a hand-manipulated tungsten electrode. The melting was performed in a water cooled copper crucible which had two 25 x 25 x 130 *mm* receptacles for separate melts. The device was equipped with a bank of four constant current welding power supplies connected in parallel and capable of providing over 3000 amps of current. A resistively heated strip of zirconium was used as an oxygen getter inside the chamber.

The chamber was evacuated to 10μm and back filled with dry nitrogen, evacuated again, and back filled with a 50/50 mixture of argon and helium to an absolute pressure of 500 *mm* of mercury. The arc was initiated using a high frequency starter with the power bank set at 20%. After the arc was established, power was then increased until the liquid metal pool was depressed under the force of the arc. This point was reached at approximately 80% power. The electrode was worked back and forth until all of the material was melted and well mixed. After the power was shut off, the chamber was purged with helium, to assist cooling, for approximately 20 minutes, evacuated with the roughing pump to remove metallic vapors, and then equalized to atmospheric pressure.

The Dry Sand Rubber Wheel specimens were cut to a length of 75 mm by removing both ends of the bars with an abrasive cut-off saw. The specimens were then ground to the nominal dimensions of 25 *mm* wide and 12 *mm* thick using a surface grinder with a magnetic chuck. One end piece was mounted and prepared for metallographic examination and the other was used to prepare X-ray specimens.

3.2.2 Chromium Alloys

The chromium white iron Dry Sand Rubber Wheel specimens were cut from thermo-mechanical pulping refiner plates. These are castings used in a pulping process for the paper making industry. The plates were approximately 30 x 40 *cm* and are about 3 *cm* maximum thickness. The pieces were cut from large reinforcement ribs on the sides of the plates and were ground to size and finish as described in section 3.1.1.

Table 3.2: Cr-Alloy Composition (%)

Chemistry	C	Cr	Mn	Si	Ni	Mo	V	Cu
Cr Iron #1	3.0	20.0	0.8	0.7	0.3	2.5	0.05	1.0
Cr Iron #3	2.8	18.0	1.2	0.7	0.4	0.5	0.05	1.0
Arc-Cr Iron	3.1	21.0	0.6	0.6	0.3	2.4	0.05	1.0
440C Steel	1.0	17.0	0.7	1.0	1.5	0.5	-	-
D2 Steel	1.5	12.0	0.6	0.6	0.3	1.0	1.0	-

The commercial chromium alloys used in this study included two 20-2-1 white irons, a 440C stainless steel derivative, and a D2 tool steel, Table 3.2. The 20-2-1 material is a class of white irons which contain nominally 20% chromium, 2% molybdenum, and 1% copper. They typically consist of a coarse lamellar eutectic with an austenitic matrix in the as cast condition as shown in Figure 3.1 and a martensitic matrix with primary and secondary carbides when heat treated, Figure 3.2. The first chromium white iron was tested in the as cast condition, designated Cr Iron #1, and the heat treated condition, designated Cr Iron #2. The heat treatment consisted of an austenization above 1000°C, air quench, and a 250°C temper. The second chromium white iron was designated Cr Iron #3 and was only tested in the as cast condition. A sample of Cr Iron #1 was re-melted in the arc furnace to generate a similar microstructure to that of the experimental molybdenum alloys, Figure 3.3. With the quick chill created by the water cooled copper crucible, the microconstituents in the arc melted alloy were very small relative to the original sand cast structures.

The 440C steel is nominally a 1% carbon, 17% chromium wrought alloy which has been adapted as a casting alloy by the refiner plate manufacturers. It is typically used in the quenched and tempered condition, however, the material does not respond well to heat treatment and often has significant amount of retained austenite. The microstructure, Figure 3.4, consists of dendrites with interdendritic eutectic carbides. The D2 steel is a standard wrought tool steel which depends on discrete secondary carbides and a tempered martensitic matrix for its wear resistance, Figure 3.5.

3.3 Metallography

The metallography specimens were mounted in epoxy filled thermoplastic mounting compound. Metallographic grinding was performed in the usual manner using silicon carbide grinding papers. Rough polishing was carried out using diamond paste on nylon cloth and a final polish with a solution of sodium hydroxide and 0.05 μm alumina on a neoprene pad. Each specimen was treated with various etchants for the metallographic examination and to identify microconstituents. Stain etchants, Table 3.3, were used assist in the identification microconstituents. The microstructures were also examined using a 2% picric acid solution.

Table 3.3: Metallographic Etchants, [20]

Etchant	Microconstituents	
Picric Acid	Delineate all carbides and intermetallics	
Murakami's Etch	ξ	slightly stained brown
	Mo_2C	delineated but not stained
	M_6C, μ	easily stained brown
Alkaline Sodium Picrate	Fe_3C, M_6C, ξ, μ	slightly stained brown
	Mo_2C	not changed
Potassium Permanganate	Mo_2C, M_6C, μ	colored to brown

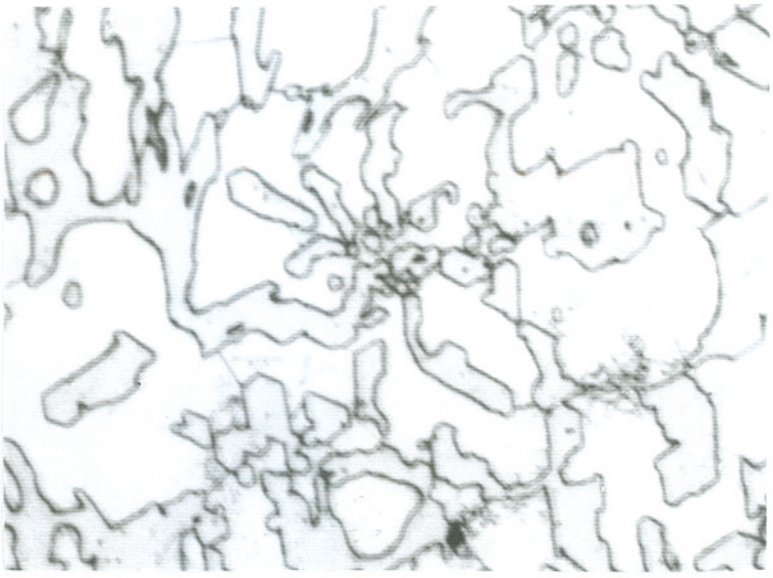

Figure 3.1 As cast 20-2-1 chromium white iron alloy, Cr Iron #1. The white non-etched phase is carbide and the gray phase is the austenitic matrix. 1000X.

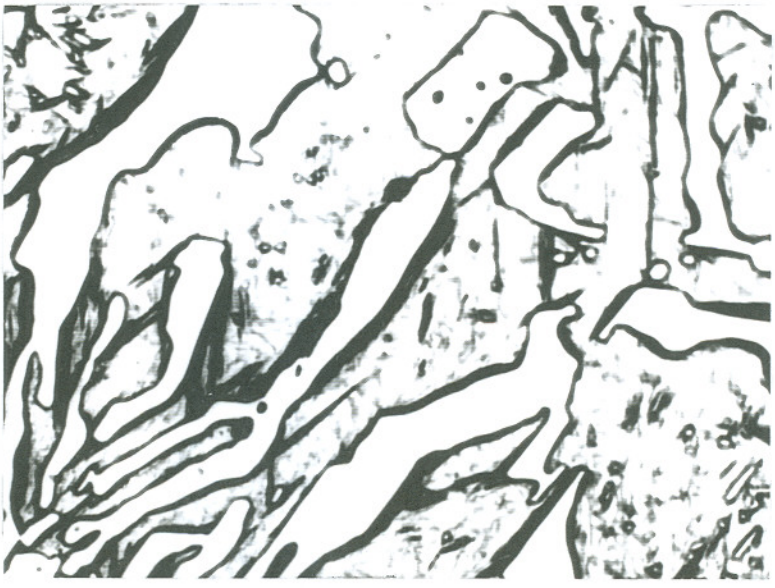

Figure 3.2 Heat treated 20-2-1 chromium iron alloy, Cr Iron #2. The non-etched phase is carbide and the dark etched phase is the martensitic matrix. 1000X.

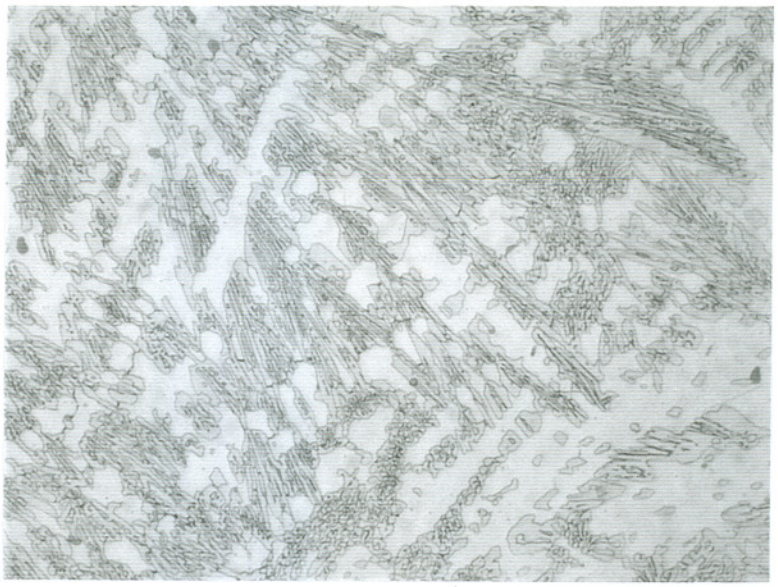

Figure 3.3 Re-melted as-cast 20-2-1 chromium iron alloy, Arc-Cr Iron. Contains primary carbide dendrites surrounded by a eutectic of austenite and carbide. 1000X.

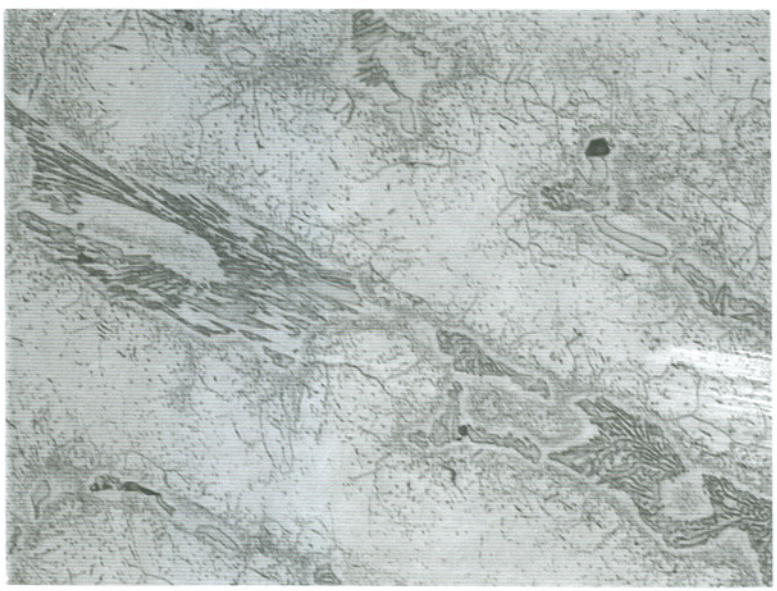

Figure 3.4 440C ferritic stainless steel. Contains large dendrites of retained austenite and martensite with interdedritic eutectic carbide. 1000X.

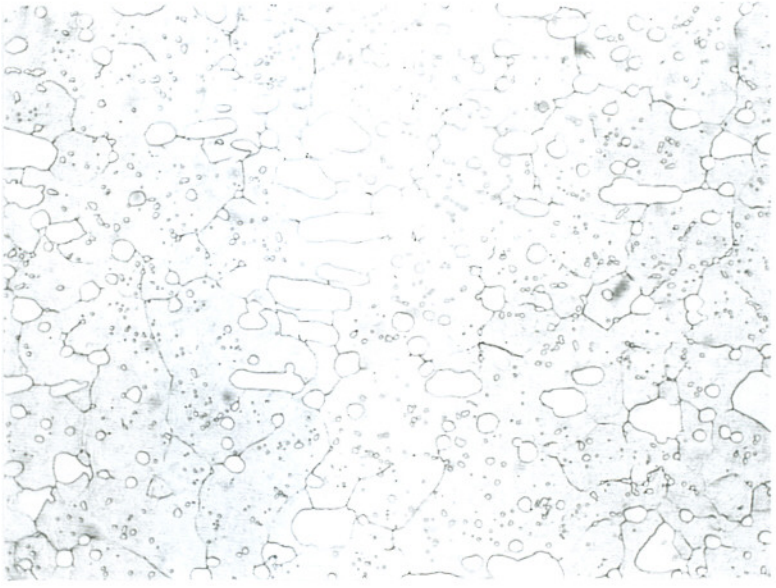

Figure 3.5 D2 tool steel. A tempered martensitic wrought alloy with discrete secondary carbides. 1000X.

3.4 Hardness Measurements

Macrohardness measurements were taken with a Rockwell hardness tester using the C-scale (HR_C). Standard test blocks were used to check the calibration of the machine prior to taking measurements. Test blocks were chosen according to the hardness range of the test sample. Averages are reported for each alloy.

3.5 Wear Testing

A Dry Sand Rubber Wheel abrasive wear test machine, ASTM Designation G65-80, was used for this work, Figure 3.6. The test incorporates a 230 millimeter diameter chlorobutyl rubber wheel which is run at 200 revolutions per minute against a standard specimen of 12 x 25 x 75 *mm*. The specimen is held by a lever arm against the rubber wheel with a load of 130 Newtons. A 200-300 μm rounded quartz test sand (AFS 50/70) flows through a nozzle in between the specimen and the wheel at a rate of 250 to 350 grams per minute.

For highly abrasion resistant materials, the ASTM standard method-A is recommended where a volume loss is to be measured after 2000 revolutions. This procedure was modified in order to calculate steady state wear rates by taking a weight loss measurement every 200 revolutions up to a maximum of 1000 revolutions. The wear rates were calculated for each wear test specimen based on weight loss alone as the density differences between the materials is not sufficient to warrant a volume loss conversion. The wear specimens were then examined in the SEM to evaluate the primary mechanisms of material removal in the wear scars.

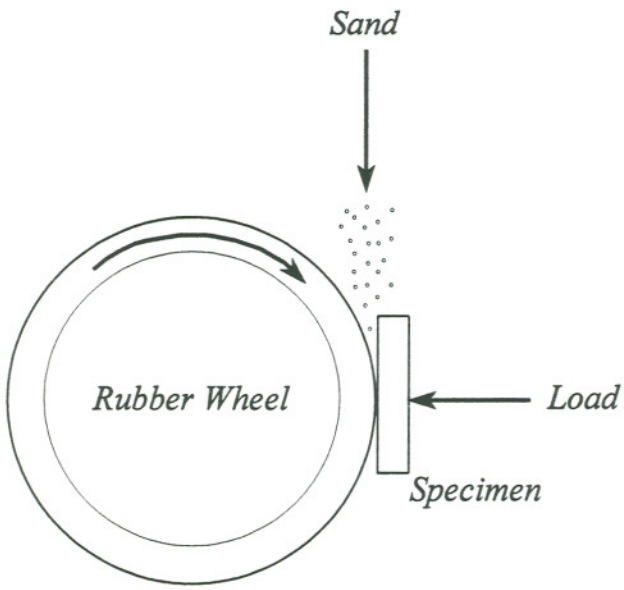

Figure 3.6 An illustration of the ASTM Dry Sand Rubber Wheel abrasive wear test.

3.6 X-Ray Analysis

Two different means of X-Ray analysis were utilized including two dissolution methods and two different diffractometers. The first diffractometer was not configured ideally for analysis of powders and did not have analytical software capabilities to identify compounds. The second effort was performed by the Bureau of Mines, Albany, Oregon, using equipment specifically configured for powder diffraction and identification of compounds. An alternate dissolution method was employed as well. Only alloys #4, #5, #7, and #8 were analyzed for phase constituents. The four alloys were selected because they were thought to contain all of the predicted phases in the ternary system.

3.6.1 First Analysis

X-Ray analysis was performed using a Siemens Kristalloflex, model D500, powder diffractometer with a Cu-Kα target and a nickel filter. The primary and secondary window sizes were 0.018° and 0.10° respectively for slow scans at 0.009°/step and 3 sec/step dwell time. Faster scans were performed at 0.05°/step and 1 sec/step dwell time with primary and secondary window sizes of 0.1 and 0.1. Window sizes were selected to minimize the noise level in the data. Specimens were first scanned quickly over a wide range of angles to identify areas of interest. Subsequent scans were performed at the slow scan rate and over a smaller range of angles.

The powders were produced by repeatedly soaking small pieces of the experimental alloys in a 10% solution of bromine and ethanol. The residue on the specimens was then scraped onto a piece of filter paper using a chrome plated spatula. The powder specimens were sprinkled onto a small piece of double-sided tape placed on a specimen holder which was aligned in the goniometer. The X-Ray data were analyzed using Siemens proprietary software package. The system identifies peaks and calculates the 2θ angles, the d-spacings and the relative intensities for each peak. The identification of unknowns was performed manually using the published d-spacings for various compounds [45].

3.6.2 Second Analysis

A Phillips model PW-1700 powder diffractometer was used with a copper X-ray tube and a graphite monochronometer. Specimens were scanned from 2θ angles of 5° to 80° at a rate of 0.02° per second.

Powders were obtained using an electrolytic method. Alloy specimens were wound with platinum wire and placed in a beaker containing an electrolyte which was a 10% solution of hydrochloric acid and ethanol. A platinum cathode was placed adjacent to the specimen and a potential of 6 volts was applied to the cell. As the dissolution progressed, a coating of reaction products would build up on the specimen. Periodically, after 5 to 10 minutes of operation, the entire cell was placed in an ultrasonic cleaner to mechanically remove the coating from the specimen and to get the reaction products suspended in the electrolyte. This sequence was repeated up to 4 times. The electrolyte was then filtered in a ceramic suction funnel apparatus using a glass microfiber filter. The filtrates were dried and analyzed in place on the filters. Indexing and phase identification was performed using a Phillips proprietary software package.

3.7 Volume Fraction Carbides

The carbide volume fraction was determined according to ASTM E562-83, manual point count, and using a Leco model 2001 Image Analyzer. The image analyzer operated from a Nikon Epiphot metallurgical microscope equipped with a digital video camera and capable of magnifications up to 1000X with an oil immersion lens. Images from the camera were captured by the image analyzer for analysis. The specimens were etched in Villella's reagent prior to the determination of carbide volume fraction. In many cases, the optical microscope could not adequately resolve the fine eutectic carbides. As a result, manual point counts were done on a Ziess model 960 Scanning Electron Microscope (SEM) at magnifications of 400X to 8000X.

The manual point count method was performed on the SEM by overlaying a grid of points systematically over the microstructure as viewed on the display monitor. To avoid bias, the operator avoids looking at the image screen when moving to a new field and the movements are gaged such that the entire specimen surface is covered. Each point that falls within the phase of interest is counted as one, and each point that falls on the edge of the phase is counted as one-half. The percentage of the average number of points counted per field is calculated based on the total number of points in the grid. If the procedure is performed in a systematic and unbiased manner, the calculated percentage represents a volume fraction of the phase.

CHAPTER 4.
RESULTS

4.1 Molybdenum Alloy Composition

The measured compositions for the experimental molybdenum alloys are listed in Table 4.1. The carbon contents for the experimental molybdenum steels and irons are suspect as described in section 3.1. Segregation may also be a possibility as indicated by the measured molybdenum contents in Alloys #4 and #8, and the carbon content of the Arc-Cr iron. The molybdenum compositions for alloys #4 and #8 registered higher than the percentage of molybdenum in the original blended powders. The carbon content of the Arc melted chromium iron was also greater than that of the original alloy.

Table 4.1: Mo-Alloy Compositions

Identification	C%	Mo%	Fe%
Alloy #2	0.1	21	balance
Alloy #3	0.1	24	-
Alloy #4	0.4	38	-
Alloy #5	1.7	18	-
Alloy #6	2.5	18	-
Alloy #7	2.7	25	-
Alloy #8	3.0	32	-

4.2 Metallographic Examination

The alloy microstructures are described in detail relative to what is seen metallographically using optical and SEM microscopy and with reference to the available phase diagrams. All of the experimental molybdenum materials are strongly magnetic indicating a significant amount of ferrite.

4.2.1 Alloy #2 Composition: 0.1% C, 21% Mo, balance iron

The microstructure, Figure 4.1 and 4.2, consists of a variegated matrix phase surrounded by a secondary precipitate at the grain boundaries. The matrix appears to include an extremely fine secondary phase. Because Murakami's stain reagent was used in preparing the metallographic specimen in Figure 4.1, the grain boundary phase appears dark in the photomicrograph. As given in Table 3.3, Murakami's etch stains the M_6C and Fe_3Mo_2 phases dark. Figure 4.2 presents a much clearer image of the matrix and the grain boundary material. Here, it can be seen that there are stained and un-stained phases in the matrix material and an apparent chemically depleted zone adjacent to the grain boundaries. The alkaline sodium picrate is known to did not stain the grain boundary phase in this case, however, the stain etchants were found occasionally to be unreliable. An intermetallic stained dark by the Murakami's would certainly be expected to be stained by the alkaline sodium picrate. With the high molybdenum and low carbon chemistry, the bulk of the alloy would be ferrite and intermetallic with no carbidic phase present.

4.2.2 Alloy #3 Composition: 0.1% C, 24% Mo, balance iron

Alloy #3 was intended to have a higher carbon content than Alloy #2, but because of alloy losses during melting, the chemistries are very similar. The microstructures, however, are very different. Alloy #3 consists of a fine secondary phase that covers the grains and the grain boundaries, Figure 4.3. The alkaline sodium picrate generated a brown stain on the secondary material and revealed another lightly etched phase beneath the obvious dark one,

indicating that it is a product of a prior solid state reaction such as the secondary Fe_3Mo_2 transforming to Fe_2Mo. Applications of Murakami's etchant to the specimen also stained the secondary phase particles a more uniform shade and did not indicate the presence of another secondary phase The possible phases based on the response of the etchants are again the M_6C carbide and Fe_3Mo_2 intermetallic. With the low carbon content in this alloy, the carbide phase is doubtful.

4.2.3 Alloy #4 Composition: 0.4% C, 38% Mo, balance iron

Two primary phases are present in Alloy #4, Figure 4.4. The first is the largest of the phases which in turn shows evidence of a secondary decomposition reaction. The initial solidification for this alloy is in the intermetallic Fe_5Mo_3 (*R*-phase) field. The Murakami's reagent has stained the primary phases a lighter shade and the secondary reaction products are dark in the photomicrograph in Figure 4.4. This phase change is undoubtably due to the peritectoid decomposition of the *R*-phase to the Fe_3Mo_2, which can also be seen along the interfaces of some of the large primary phase material in Figure 4.5. The remaining liquid then begins to form α-Fe and M_6C carbide which may be the finer, globular, primary phase in the photomicrograph. This is uncertain as the 0.4% carbon would not be expected to be enough to precipitate a significant carbide volume fraction. Nothing was found in the literature indicating that the *R*-phase would be colored by any of the etchants used.

4.2.4 Alloy #5 Composition: 1.7% C, 18% Mo, balance iron

The alloy, Figure 4.6, first solidified as primary austenite [21,23] or delta ferrite [22]. A portion of the austenite passes through the two phase field involving γ-Fe and Mo_2C carbide as seen on the 1000°C isotherm, Figure 2.5. Large martensitic laths were found in many of the dendrites. The interdendritic region consisted of the ternary eutectic with a lamellar morphology. The eutectic is too fine to determine if any of the microconstituents were colored by the stain reagents or to determine if the ξ-carbide phase is present.

4.2.5 Alloy #6 Composition: 2.5% C, 18% Mo, balance iron

This alloy follows a solidification path similar to Alloy #5 except that the first material to crystallize maybe austenite. The higher carbon content placed Alloy #6 significantly closer to the ternary eutectic which produced more interdendritic eutectic and an overall greater carbide volume fraction, Figure 4.7. This eutectic is also too fine to resolve any staining of the microconstituents.

4.2.6 Alloy #7 Composition: 2.7% C, 25% Mo, balance iron

The first material to solidify was the primary M_6C carbide and austenite. The remaining liquid then formed austenite and Mo_2C before the lamellar ternary eutectic reaction with γ-Fe, Mo_2C, and M_3C. All of the primary carbides have a similar tint after etching with potassium permanganate and have a clear delineated region surrounding them, Figure 4.8. This moat surrounding the primary phase has the appearance of a peritectic or peritectoid type reaction. Many of the smaller discrete phases have a more rounded shape indicating that they may be the result of a secondary reaction product. Other smaller carbides are too coarse to be eutectic, but appear as a non-uniform lamellar phase also indicating a secondary reaction. In Alloy #4, the finer, globular phase was thought to be the M_6C carbide. Here, the obvious primary M_6C is much more massive and angular.

Dendrites of retained austenite with lathe martensite are intertwined with the carbides and the lamellar eutectic. In between some of the dendrite arms, a dark-staining variegated phase is present which cannot be resolved optically at a magnification of 1000X. The eutectic stained dark in some cases and did not stain in others. There may be some differences between the two eutectic carbides, Mo_2C and M_3C, but they were also difficult to resolve at this magnification. Again it cannot be determined if any ξ-carbide is present.

4.2.7 Alloy #8 Composition: 3.0% C, 32% Mo, balance iron

The alloy is comprised of a relatively fine microstructure with a few blocky primary carbides, an irregular lamellar transformation phase, and a slightly more coarse lamellar eutectic, Figure 4.9. It begins solidification as either primary M_6C [21,23] or Mo_2C [22], and passes through a γ-Fe and Mo_2C reaction, and finally the ternary eutectic reaction forming γ-Fe, Mo_2C, and M_3C.

Some of the primary carbides stained dark with the Murakami's and some did not. The Mo_2C carbide should not stain with this reagent. However, the Mo_2C is said to be stringy or rod-like in shape as given in Table 2.3 [14]. This description may fit the elongated primary phase found in Alloy #8. The lamellar eutectic was slightly tinted in some areas and stained dark in others. The difference between the two eutectic carbides may be the Mo_2C and M_3C phases. There also appear to be occasional dendrites of retained austenite with lathe martensite.

Figure 4.10 is an SEM micrograph of a carbide that has undergone a subsequent transformation. This is obviously primary material, Mo_2C or M_6C, which has been transformed to the irregular lamellar morphology described above. An EDX analysis on a metallographic specimen generated the average results given in Table 4.3. The primary phase indicated is a strong candidate for the Mo_2C carbide because of its high molybdenum content.

Table 4.2: EDX Data, Alloy #8

Microconsituent	Mo%	Fe%
Primary Phase	93	7
Irregular Lamellar	73	27
Matrix Phase	6	94

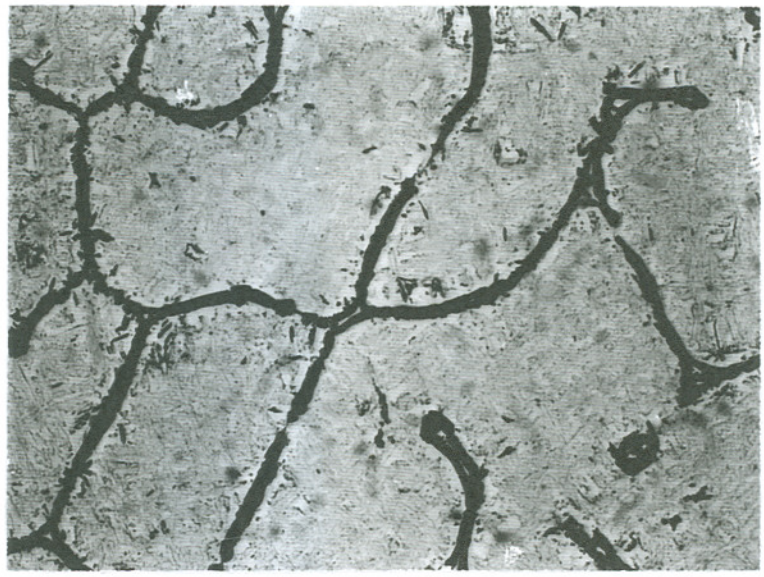

Figure 4.1 Alloy #2 prepared with Murakami's stain reagent. The stain etchant darkened the grain boundary intermetallic. 1000X.

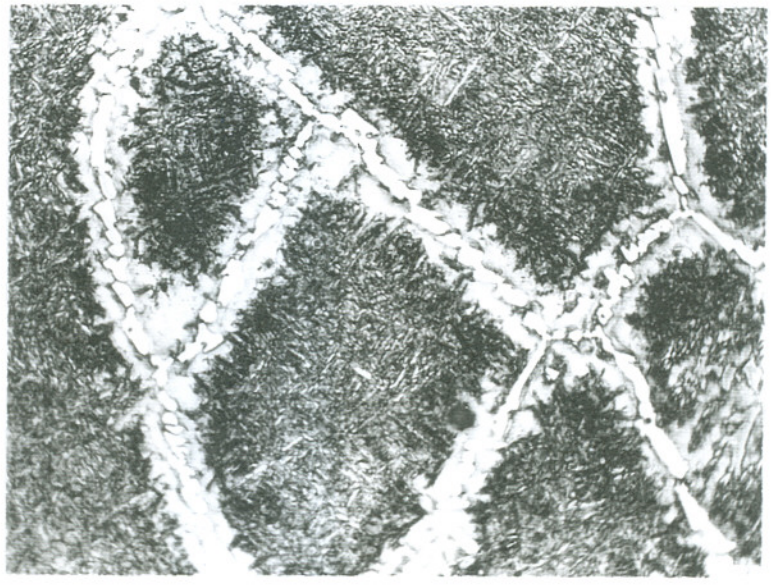

Figure 4.2 Alloy #2, prepared with alkaline sodium picrate stain reagent. The unetched grain boundary intermetallic can be seen with the adjacent depleted zone. 1000X.

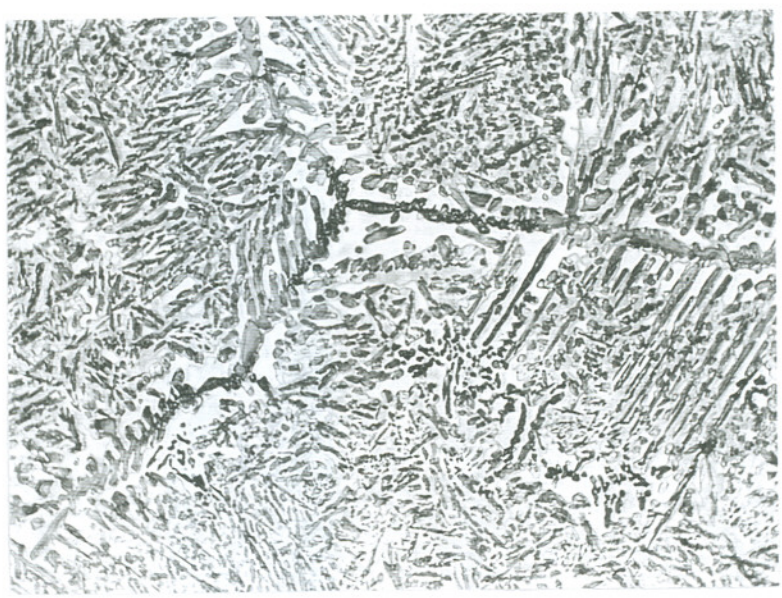

Figure 4.3 Alloy #3, prepared with alkaline sodium picrate stain reagent. The stained intermetallic precipitate can be seen in the grains and on the grain boundaries. 1000X.

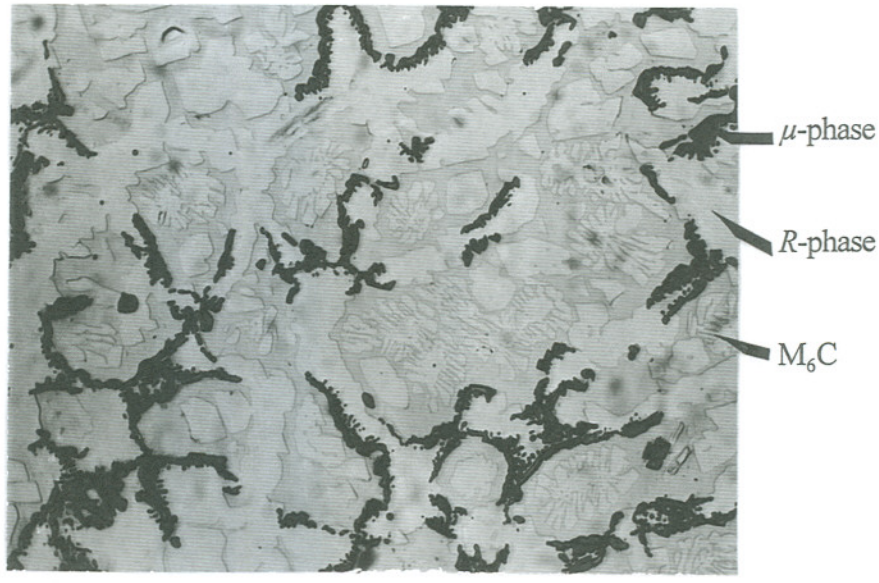

Figure 4.4 Alloy #4, prepared with Murakami's stain reagent. Contains primary intermetallic *R*-phase which has experienced a peritectoid decomposition (μ-phase) and possible M_6C carbides. 1000X.

Figure 4.5 Alloy #4, prepared with picric acid showing a peritectoid reaction product. 1000X.

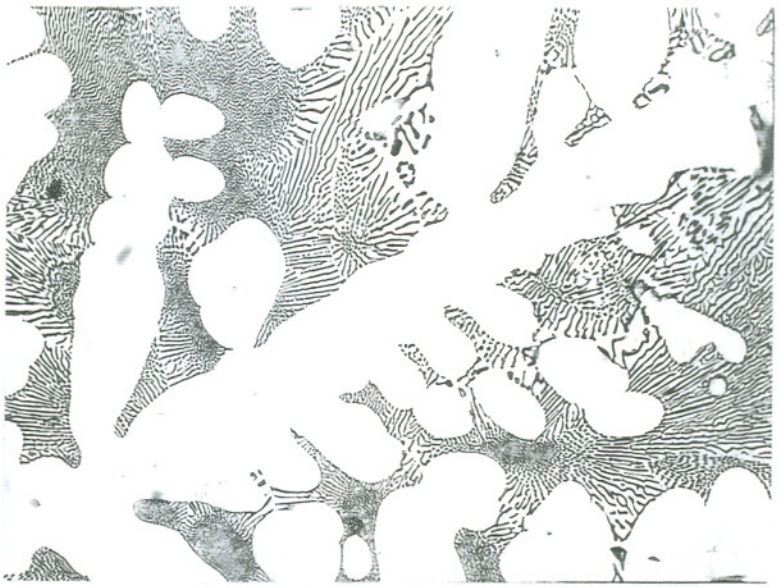

Figure 4.6 Alloy #5, prepared with Murakami's stain reagent. Consists of austenitic dendrites with interdendritic eutectic. 1000X.

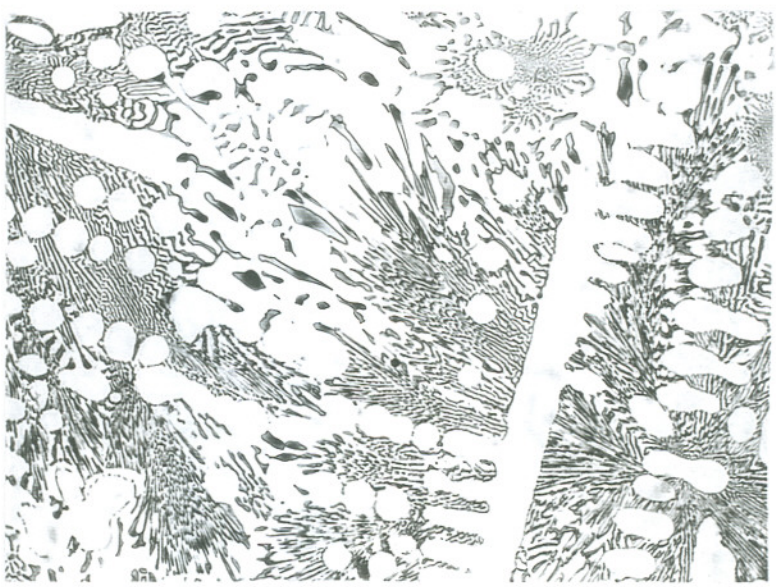

Figure 4.7 Alloy #6, prepared with Murakami's stain reagent. Contains austenitic dendrites with interdendritic eutectic. 1000X.

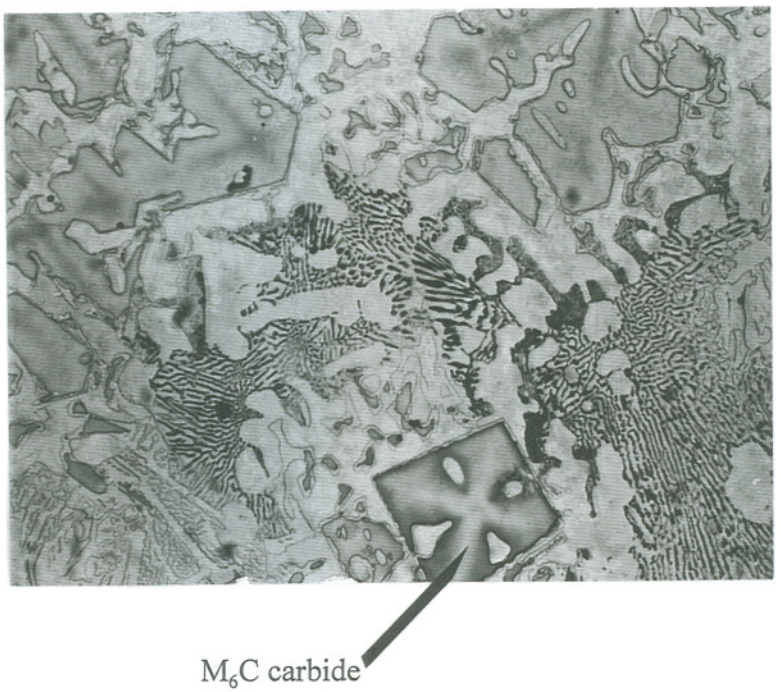

Figure 4.8 Alloy #7, prepared with potassium permanganate stain reagent. Contains large hypereutectic M_6C carbides and eutectic. 1000X.

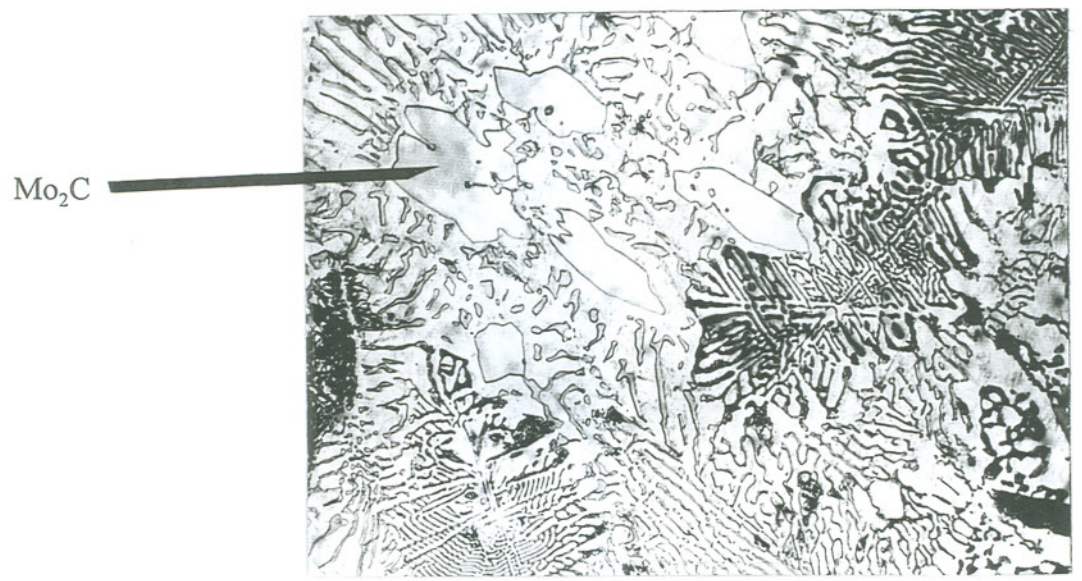

Figure 4.9 Alloy #8, prepared with Murakami's stain reagent. Shown are large primary Mo_2C carbides and eutectic. 1000X.

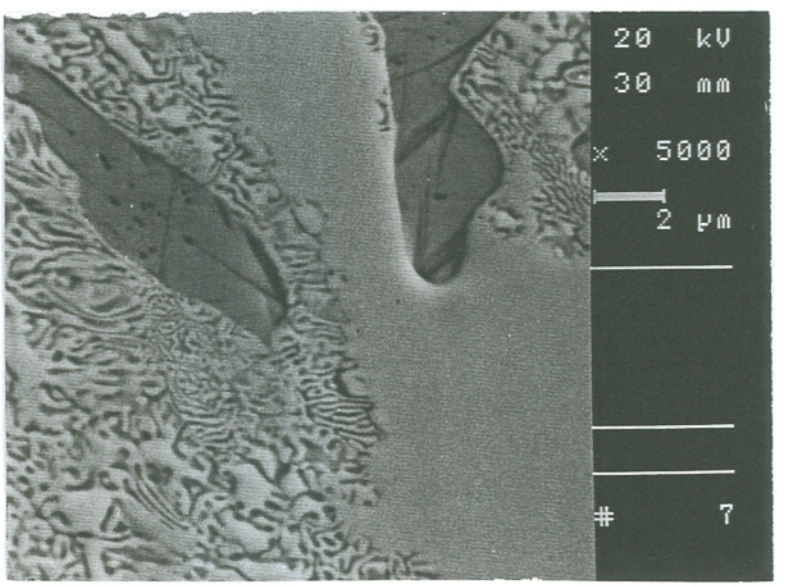

Figure 4.10 Alloy #8, An SEM micrograph showing a secondary decomposition, 5000X.

4.3 Hardness Measurements

The macrohardness measurements follow a loose trend, increasing with carbon content, from approximately HR_C 40 to 65. Table 4.3 lists the hardnesses for the experimental molybdenum alloys along with their carbon and molybdenum contents as a reference. The hardnesses given are averages for multiple indentations on a single DSRW specimen.

Table 4.3: Hardness Measurements

Alloy	%C	%Mo	HR_C
#2	0.1	21	41.6
#3	0.1	24	39.4
#4	0.4	38	50.9
#5	1.7	18	63.2
#6	2.5	18	64.8
#7	2.7	25	63.6
#8	3.0	32	64.5

Alloy	%C	%Cr	HR_C
Cr Iron #1	3.0	20	52.5
Arc-Cr Iron	3.1	21	53.4
Cr Iron #2	3.0	20	63.5
Cr Iron #3	2.8	18	49.0
440C Steel	1.0	17	56.0
D2 Steel	1.5	12	60.0

The bulk hardness of Alloy #2 is HR_C 42 which is in the range of a tempered martensite, but is too hard to be ferrite. This hardness level also suggests a microstructure containing intermetallic material. Alloy #3 is at the high end of the range for a eutectoid at HR_C 39 which would be conceivable if the carbon level was close to what was originally intended for this alloy. However, this hardness level is more likely due to the presence an intermetallic. Alloy #4 is unique among the experimental alloys in that its microstructure is mostly large amounts of intermetallic hard phase. The bulk hardness values for this alloy support this hypothesis. The hardness of the remaining white irons are in the ranges expected for these materials in the as cast condition.

4.4 Image Analysis

The image analysis data for the experimental alloys and several white iron materials are summarized in Table 4.4. Given, is a description of the phases, the hard phase volume fraction (VF), and the confidence interval (CI). The typical, fully-eutectic, iron alloys tend to be approximately 30% carbide volume fraction.

Alloy #2 developed a grain boundary intermetallic which was approximately 9% volume fraction. The measured carbon content for this material was 0.1% and therefore could not contain a meaningful carbide volume fraction. Alloy #3 was also measured with a very low carbon content. The appearance of the microstructure could be related to a non-lamellar eutectoid. Nevertheless, the stain etchants indicate an intermetallic phase consisting of over 36% of the microstructure.

The total hard phase found in alloy #4 was 59% with the intermetallic constituting 33% and various assumed carbides making up the remaining 26%. Again, the uncertainty of the carbon content is an issue, and the microstructure and X-Ray analysis strongly indicate that a carbidic phase is present. Alloys #5 and #6 were very similar with 29% and 33% eutectic carbide respectively. Alloy #6 contained a few blocky primary carbides.

Table 4.4: Volume Fraction Hard Phase

Alloy	Description	Volume Fraction (%)	Confidence Interval (%)
#2	Grain Boundary Intermetallic	9.4	6.9
#3	Dispersed Intermetallic	36.6	2.6
#4	Primary Intermetallic	33.2	3.0
	Primary Carbides	25.9	2.8
	Total Hard Phase	59.1	
#5	Eutectic Carbides	29.1	4.4
#6	Eutectic Carbides	30.3	4.3
#7	Blocky Primary Carbides	27.8	3.3
	Eutectic Carbides	24.2	4.2
	Total Hard Phase	52.0	
#8	Blocky Primary Carbides	10.7	8.1
	Eutectic Carbides	30.1	3.7
	Total Hard Phase	40.8	
Cr-Iron #1	Eutectic Carbides	28.5	2.7
Arc-Cr Iron	Blocky Primary Carbides	24.5	8.5
	Eutectic Carbides	11.6	3.0
	Total Hard Phase	36.1	
Cr Iron #2	Eutectic Carbides	33.0	2.9
Cr Iron #3	Eutectic Carbides	27.3	3.6
440C Steel	Eutectic Carbides	7.0	3.6
D2 Steel	Secondary Carbides	12.0	0.5

The microstructures of Alloys #7 and #8 were also very similar to each other. Alloy #7 contained a total of 52% carbide. Of that total, 28% were probably large primary carbides with the eutectic making up the remainder. In contrast, Alloy #8 had fewer blocky carbides, 14% volume fraction, and 30% eutectic carbides for a total of 44%. The difference between the two compositions results from their location near the M_6C and Mo_2C liquidus phase fields.

The other alloys included in Table 4.4 are the 20-2-1 white irons in the as cast and heat treated form, the 440C stainless steel alloy, and the D2 tool steel. The 20-2-1 alloys are hypoeutectic except for the Arc-Cr Iron alloy which contains some larger primary carbides as well. This is most likely due to a non-homogenous composition resulting from the arc melting process. The 440C steel contains a small amount of interdendritic eutectic carbide. The D2 material is the only wrought material and was found to have 12% secondary carbides.

4.5 X-ray Diffraction Analysis

X-ray diffraction analysis was carried out on the four alloys which would provide the most information for the iron corner of the phase diagram. It was presumed that all of the phases of interest for this work were represented in these materials. The 2θ angle versus intensity plots and tables listing matches of experimental data and peaks from the powder diffraction files [45] are included in Appendix A. A list of all phases found in the X-ray diffraction work is given in Table 4.5.

Table 4.5: X-ray Diffraction Summary

Phase	Alloy #4	Alloy #5	Alloy #7	Alloy #8
α-Fe	✔	✔		✔
M_6C	✔	✔	✔	✔
Mo_2C		✔	✔	✔
ξ-phase	✔		✔	
R-phase	✔			
μ-phase	✔			
Fe_2Mo	✔			

4.5.1 First Analysis

Alloy #4 - The results for alloy #4 were by far the most complex with scans between 2θ values of 30° to 75° showing 17 viable peaks. Six phases were found to make plausible matches for the d-spacings. Some of the peaks were hardly recognizable and would not be considered viable except that they occurred in several repeats in the same 2θ range. This was not always the case. Other peaks picked out by the computer were barely out of the baseline noise and were not found in any other repeats for that 2θ angle. These were not considered viable peaks. However, a weak match for the α-Fe peak, a phase expected in these materials, is easier to accept under these conditions.

The intermetallic diffraction data are much more confusing. Three different phases are possible here. These are Fe_3Mo_2, Fe_2Mo, and $Fe_{63}Mo_{37}$. The Fe_2Mo is a stable room temperature Laves phase [10]. The structure for the Fe_3Mo_2 and Fe_7Mo_6 phases are slightly different, but describe the same intermetallic phase. The Fe_7Mo_6 phase was not found in these data. Some indication of the primary *R*-phase was expected in the diffraction data. There was some confusion about the structure of Sinha's *R*-phase until a match was made between his diffraction data and the Powder Diffraction File. Only then was it clear that the

$Fe_{63}Mo_{37}$ and Sinha's *R*-phase were one and the same. The $Fe_{63}Mo_{37}$ phase is suspected to be the equivalent to the Fe_5Mo_3 *R*-phase. The $Fe_{63}Mo_{37}$ showed the strongest match of the intermetallics for these diffraction data. The Fe_3Mo_3C triple carbide showed a very good match with the diffraction files. The $Fe_{11}Mo_6C_5$ carbide diffraction peaks were found but did not show strong intensities. This is the ξ-phase carbide and is the same phase as the Fe_2MoC carbide.

Alloy #5 - Three strong peaks were seen, two of which were good matches for α-Fe. The third peak was a possible match for the Mo_2C or the ξ-phase carbide. It is not clear why other peaks were not present as this range of 2θ values should have included other carbide peaks.

Alloy #7 - A strong match was seen for the Mo_2C and M_6C carbides. This alloy was thought to solidify with primary M_6C and austenite and then form primary Mo_2C at a lower temperature. A weaker match was found for the ξ-phase which would be present as a result of either the ternary eutectic reaction or the ξ-phase field. In this alloy, the data matched the Fe_2MoC structure instead of the $Fe_{11}Mo_6C_5$ as was found in Alloy #4.

Alloy #8 - Only α-Fe and several other unknown peaks were revealed for the first attempt which was a very fast scan. Subsequently, two slower scans revealed many strong peaks through the same 2θ angles. A very good match was made for the Mo_2C carbide and α-Fe. A single peak corresponded to a d-spacing for the M_6C carbide which occurs at greater 2θ angles. Unfortunately no diffraction data were obtained at higher 2θ angles which included the entire M_6C 2θ range.

Molybdenum Powder - A molybdenum powder sample from the material used to make the experimental molybdenum alloys was also tested to verify the technique. The powder was labeled as 99.99% pure molybdenum. A strong match for the M_6C carbide was found in the diffraction data.

4.5.2 Second Analysis

The Bureau of Mines diffraction data was quite different as a result of the variation in extraction methods. Another variable was that a computer data acquisition system was used to analyze the data [47]. Only three separate phases were found among all four of the alloys. Because the computer data was presented in a form that could not be manually checked, it is difficult to know if one method was superior to the other.

Alloy #4, was found to have an $Fe_{63}Mo_{37}$ intermetallic and a carbide with a structure similar to that of the Co_3W_3C carbide. The Co_3W_3C is the structure for the M_6C carbide. Alloys #5, #7, and #8 were all found to contain carbides with the Co_3W_3C and Mo_2C structure.

4.6 Wear Testing

The wear test results, summarized in Table 4.6, showed the experimental molybdenum alloys with the combination of high carbon and molybdenum to be comparable to the chromium white irons. The weight loss versus sliding distance curves for the molybdenum alloys are shown in Figure 4.11. A general trend of decreasing weight loss with increasing carbon content can be seen. The four alloys with the least weight loss were all very close, but differences in wear rate can be resolved between them. These four materials had similar hardness values but very different microstructures are represented between Alloys #5 - #6 and Alloys #7 - #8.

Similar plots for the chromium alloys can be seen in Figure 4.12. The 440C alloy showed the greatest weight loss with the Arc-Cr Iron next and the white irons and the D2 tool steel grouped together with excellent wear resistance. The Arc-Cr Iron alloy was very close in composition and microstructure with Cr Iron #1 yet its wear resistance is significant less after arc melting. The wear rates of the four most wear resistant molybdenum alloys compare very favorably with the sand cast chromium white irons and the D2 tool steel.

Differences can be seen in the behavior of the molybdenum and chromium alloys in the wear rate versus bulk hardness data in Figure 4.13. Here, the wear rate of the commercial chromium alloys show little correlation with hardness. The 440C steel is an outlier on the plot with a very high wear rate for its hardness level. The carbide volume fraction value given in Table 4.6 may well be too high as a result of confusion in resolving the very fine eutectic carbides in this alloy. Data from Fulcher et al [41] are also represented in Figure 4.13. The wear rate of these alloys is independent of bulk hardness as well. The molybdenum alloys show a very clear linear relationship including Alloy #4 which contains a high intermetallic volume fraction.

The wear resistance versus carbon content data, Figure 4.14, for Fulchers materials show a weak parabolic relationship. The molybdenum alloys form a modest parabolic relationship while the commercial chromium alloys do not fit a pattern. The D2 steel and the chromium irons fit relatively well with the experimental chromium alloys but the 440C and Arc-Cr Iron materials, with the finer carbides, show much lower wear resistance.

The most widely used quantitative metallographic measurement for alloys with carbidic second phases is the carbide volume fraction. Figure 4.15 reveals the relationship between the wear rate and the carbide volume fraction for the chromium and molybdenum alloys. The data of Figure 4.15 were plotted without considering the volume fraction of the intermetallic phases. Again, the chromium alloys minus the 440C and Arc-Cr Iron materials show a very weak parabolic relationship of decreasing wear rate with increasing volume fraction to a minima at approximately 30% carbide volume fraction. The best fit for the molybdenum alloys is also a parabolic curve and the trend of decreasing wear rate with increasing carbide volume fraction is much stronger. The wear behavior of the 440C and Arc-Cr Iron materials places them on the curve with the molybdenum alloys.

Table 4.6: Summary of Results

Experimental Alloy	Carbide Volume Fraction (%)	Hardness (HR_C)	Wear Rate ($\mu g/m$)
#2	-	42	386
#3	-	39	401
#4	26	51	205
#5	29	63	104
#6	30	65	81
#7	52	64	53
#8	43	64	35
Cr Iron #1	29	52	47
Arc-Cr Iron	37	53	132
Cr Iron #2	33	64	45
Cr Iron #3	25	49	54
440C Steel	7	56	362
D2 Steel	12	60	69

The molybdenum materials seem to require a much greater carbide volume fraction to obtain the same level of wear resistance as the chromium alloys. Alloy #8 exhibits the lowest wear rate of the molybdenum alloys even though Alloy #7 has a greater carbide volume fraction. This situation is similar to that described by Fulcher et al and others [37,41] for white iron alloys. Fulcher's data was plotted on a much smaller scale which enhanced the parabolic shape. Plotted with respect to the experimental molybdenum data, the relationship does not look as strong.

4.7 DSRW Specimens

Photomicrographs from the SEM examination of the Dry Sand Rubber Wheel specimens are shown in Figures 4.16 through 4.27. It can be seen that the abrasive material has plowed through the matrix material in all cases and on some specimens craters are found resulting from fragments of material having been removed. The material removed can often be associated with some microstructural component of the alloy as is the case with Alloy's #3, #4, and the Arc-Cr Iron specimen. Occasional large blocky second phase particles show evidence of fracture and spalling as can be seen with Alloy #7.

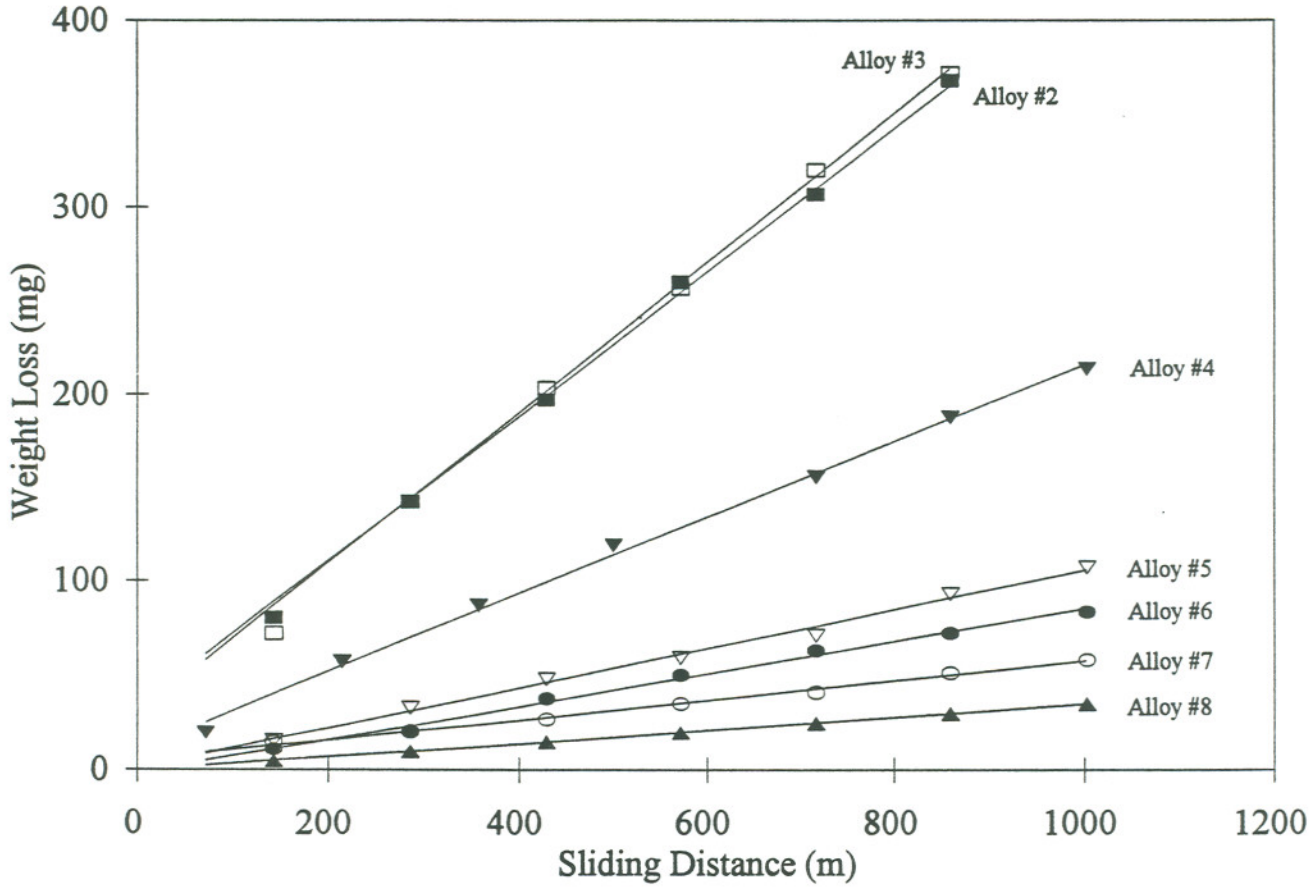

Figure 4.11 Sliding distance versus weight loss curves for the eight experimental molybdenum alloys.

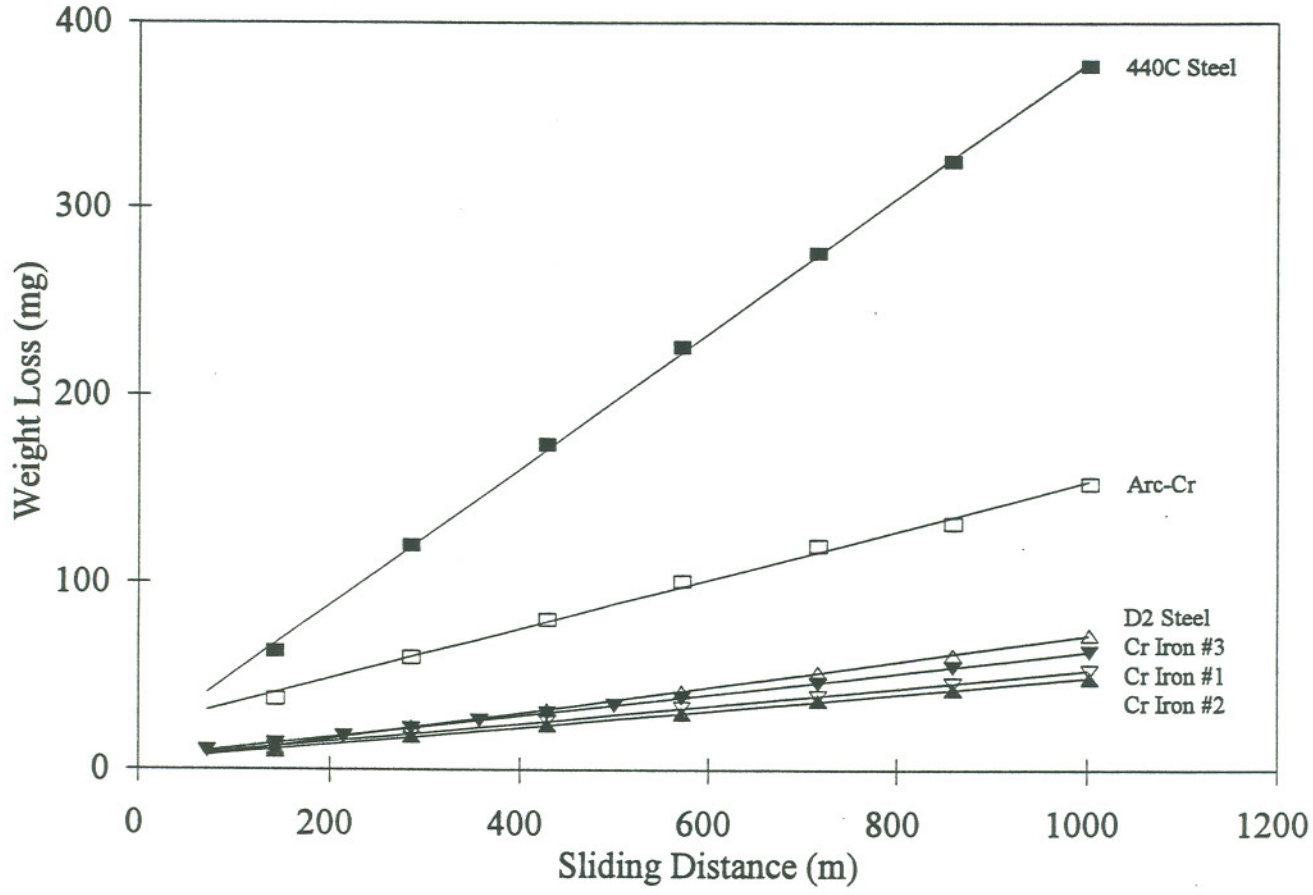

Figure 4.12 Sliding distance versus weight loss curves for the experimental and commercial chromium alloys.

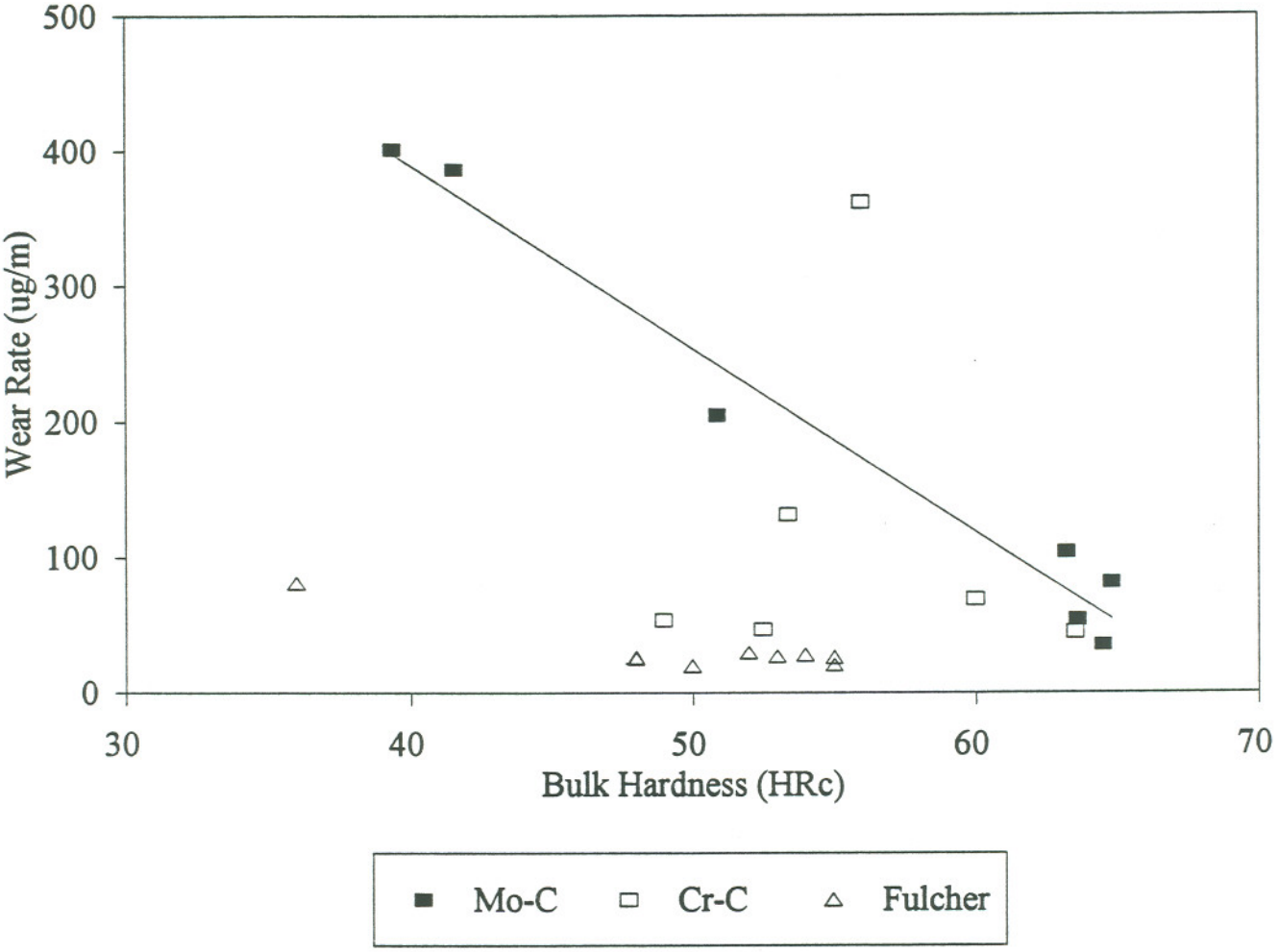

Figure 4.13 Wear rate versus hardness data for the commercial and experimental chromium and molybdenum alloys. The curve fit is for the molybdenum alloy data only.

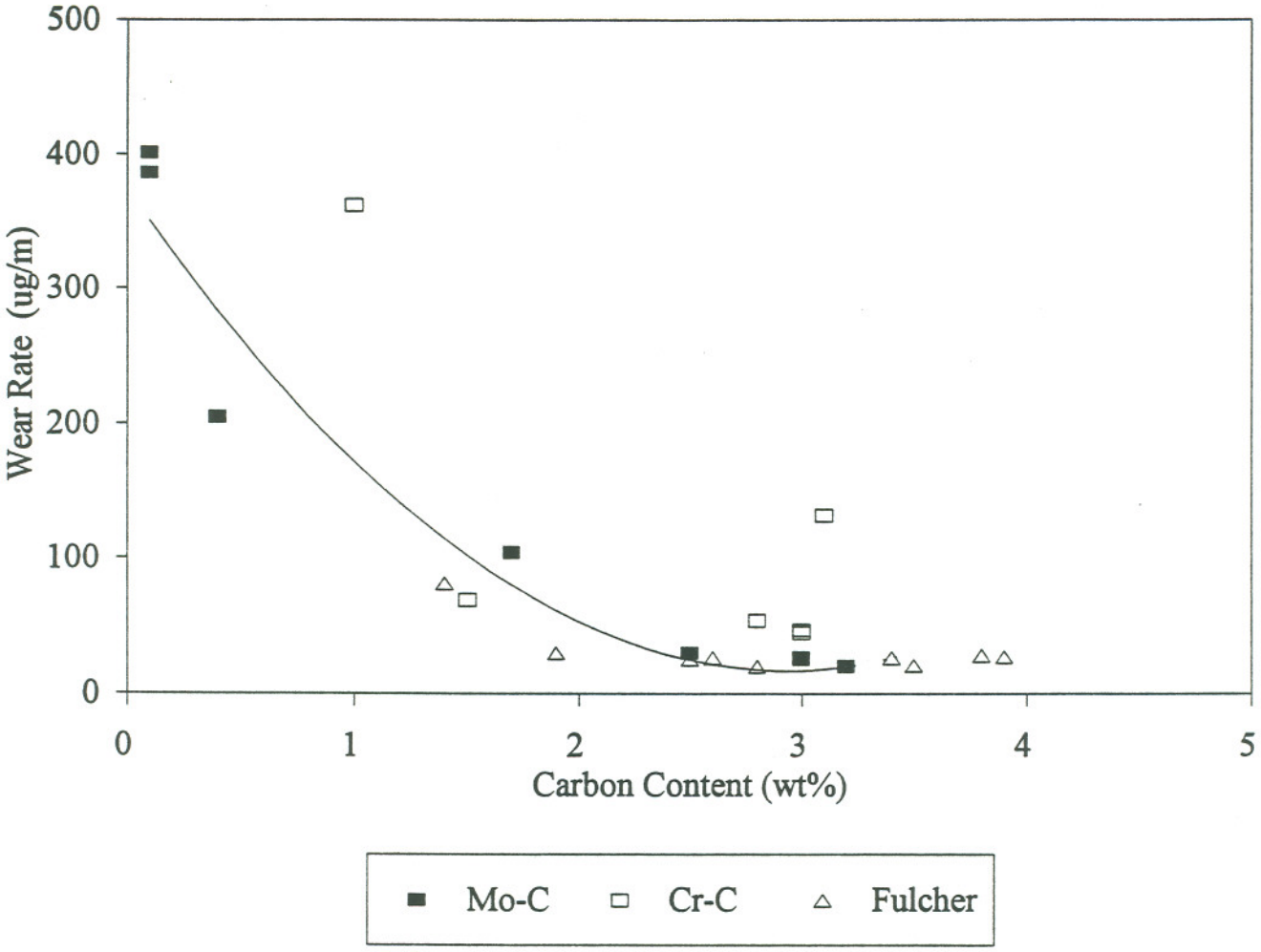

Figure 4.14 Wear rate versus carbon content data for the commercial and experimental chromium and molybdenum alloys. The curve fit is for the molybdenum alloy data only.

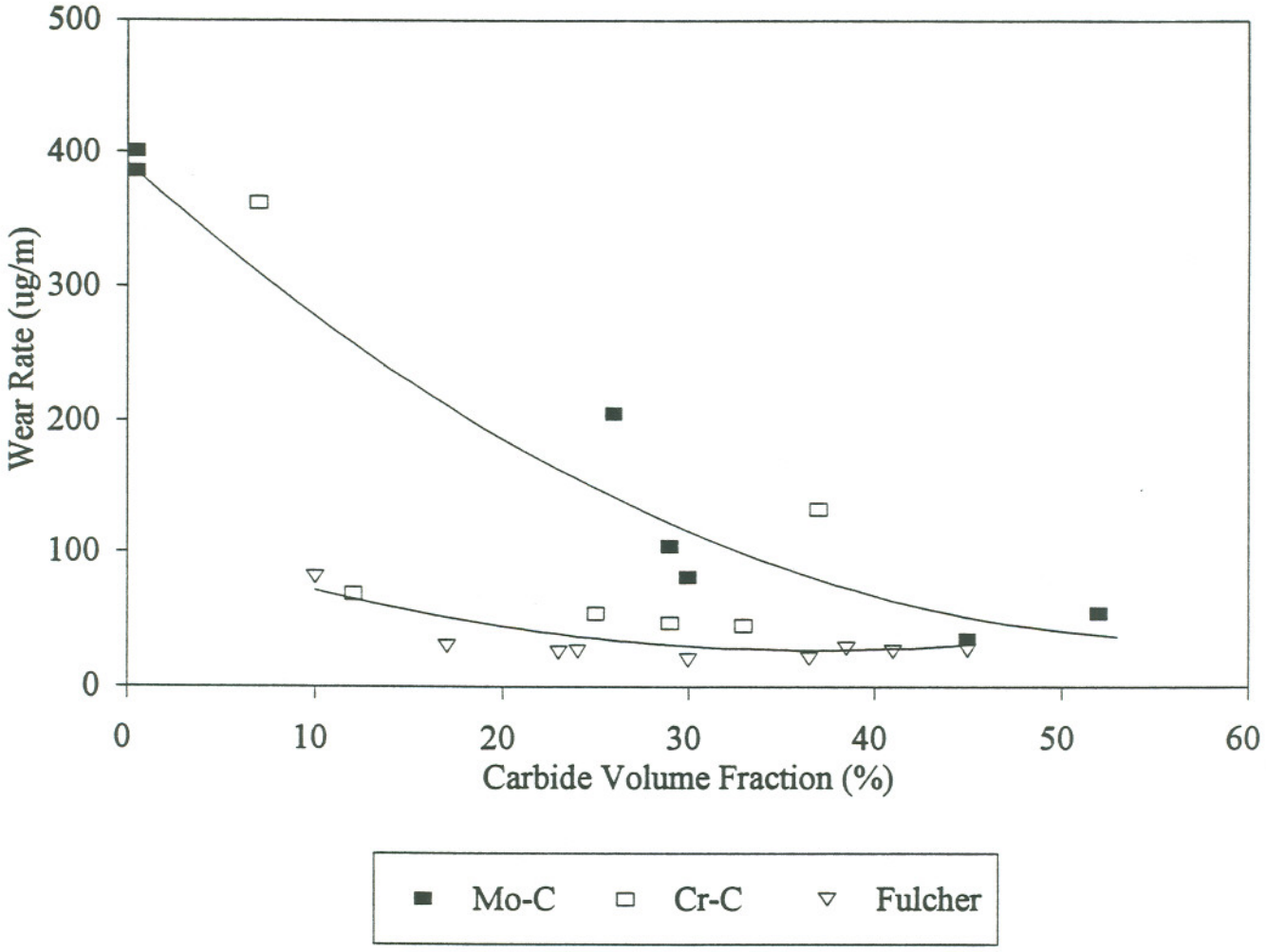

Figure 4.15 Carbide volume fraction versus wear rate for the commercial and experimental chromium and molybdenum alloys. The curve fit is for the molybdenum alloy data only.

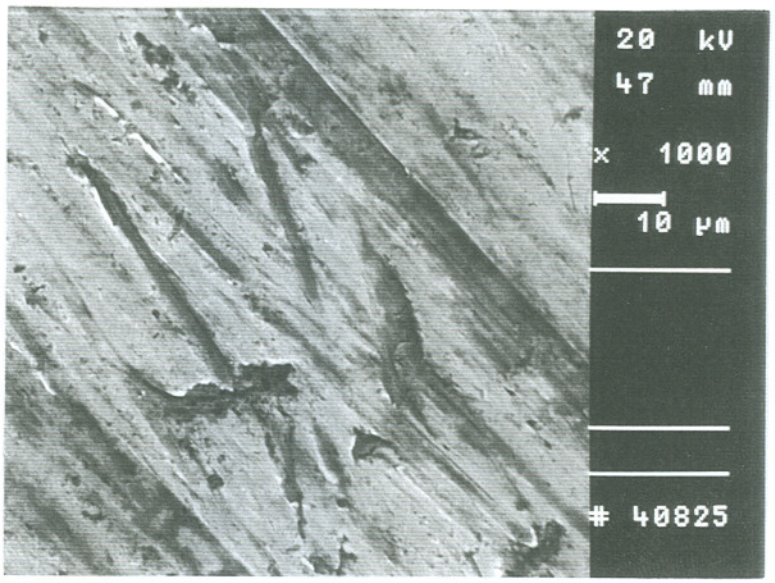

Figure 4.16 Alloy #2, Dry Sand Rubber Wheel specimen wear scar, 1000X.

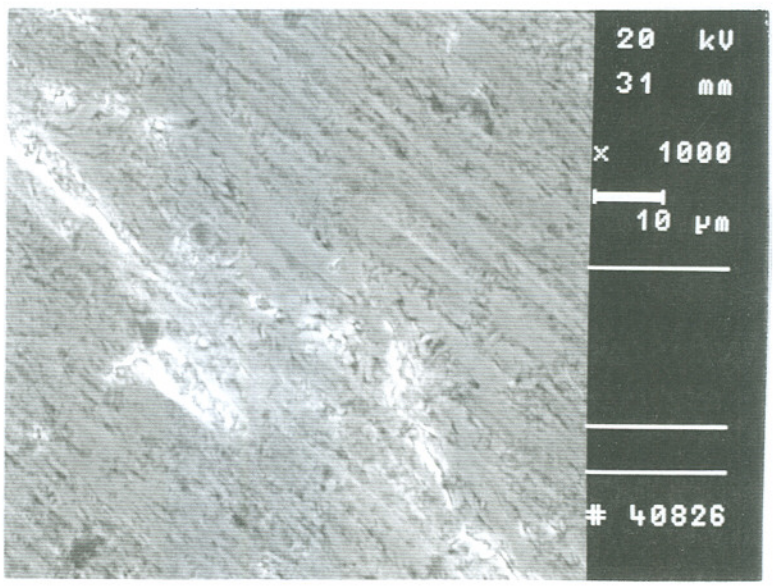

Figure 4.17 Alloy #3, Dry Sand Rubber Wheel specimen wear scar, 1000X.

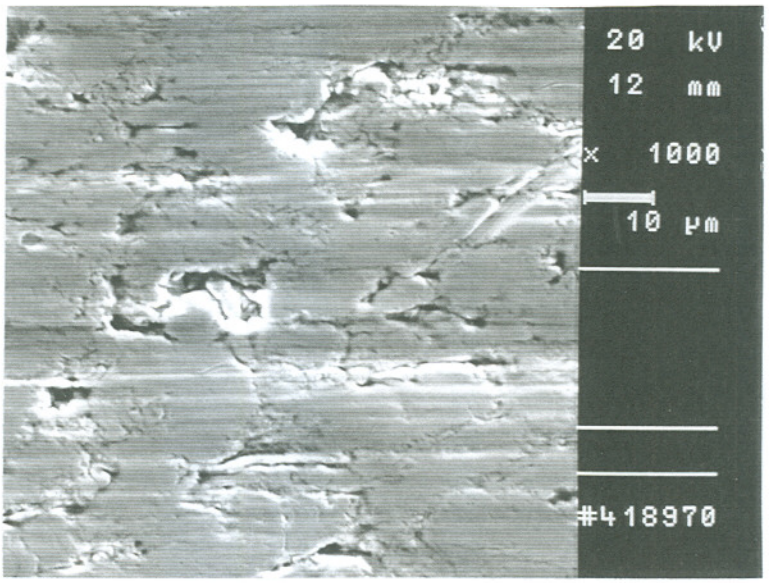

Figure 4.18 Alloy #4, Dry Sand Rubber Wheel specimen wear scar, 1000X.

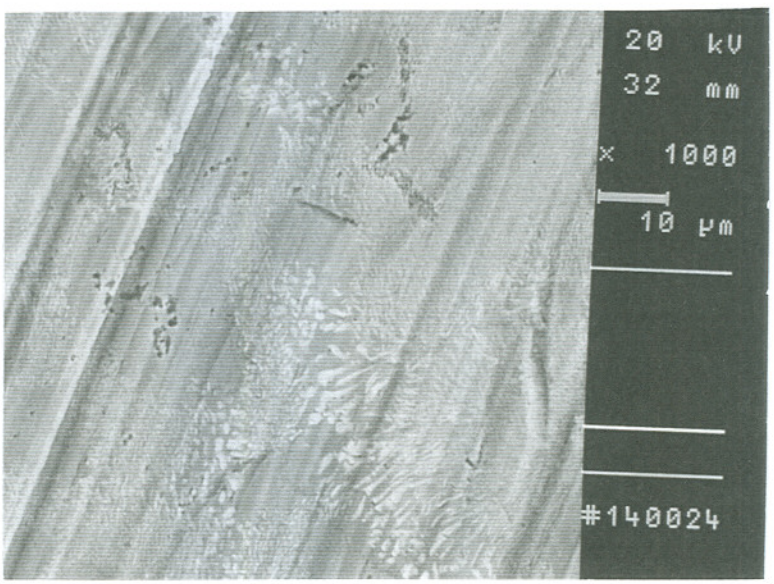

Figure 4.19 Alloy #5, Dry Sand Rubber Wheel specimen wear scar, 1000X.

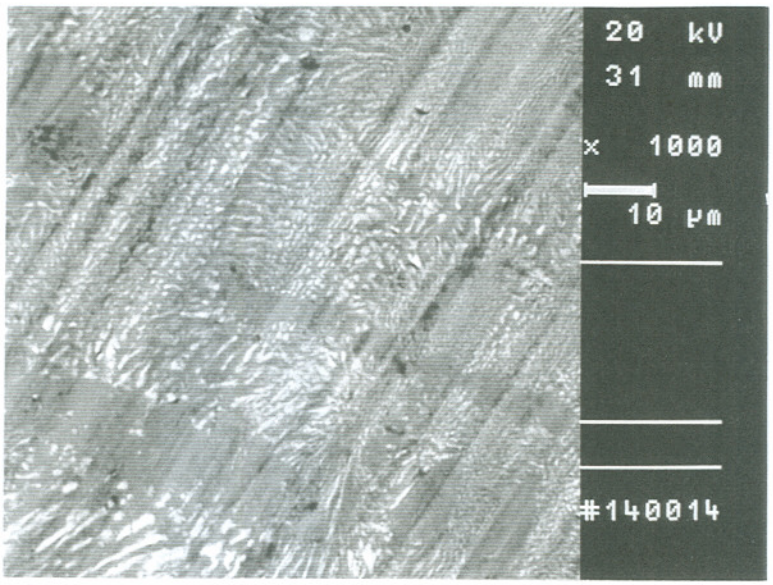

Figure 4.20 Alloy #6, Dry Sand Rubber Wheel specimen wear scar, 1000X.

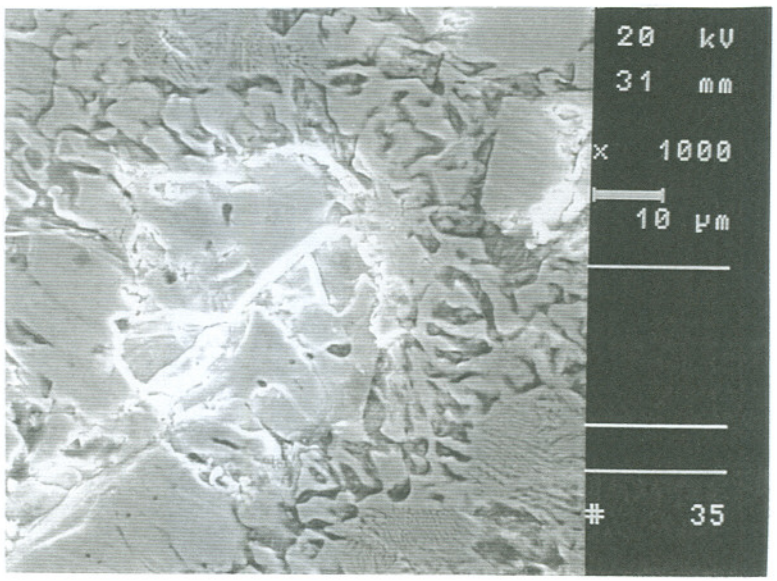

Figure 4.21 Alloy #7, Dry Sand Rubber Wheel specimen wear scar, 1000X.

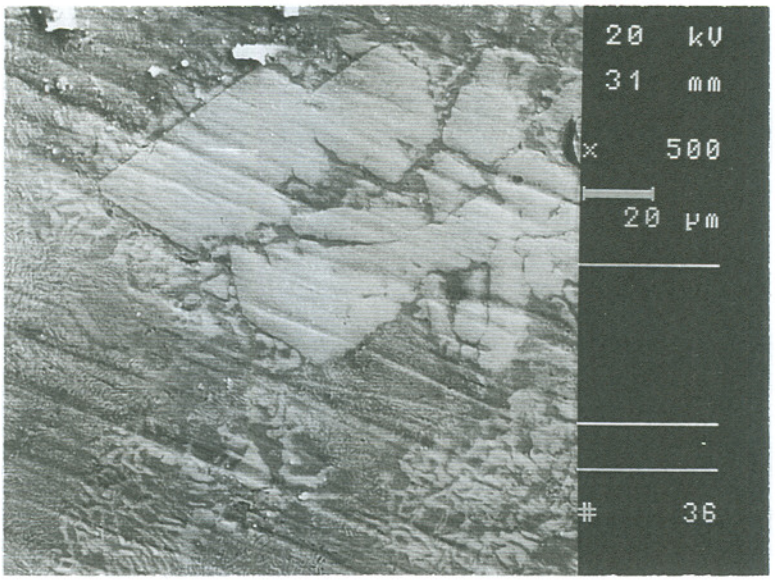

Figure 4.22 Alloy #8, Dry Sand Rubber Wheel specimen wear scar, 1000X.

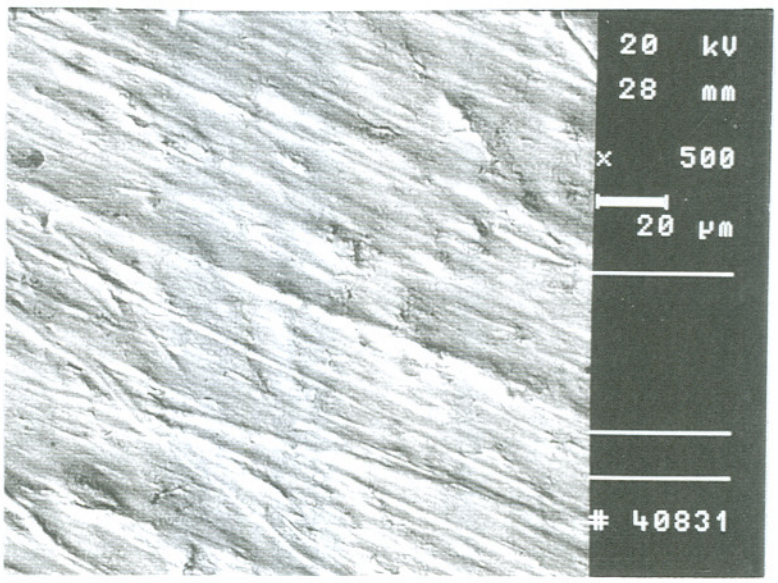

Figure 4.23 As cast Cr Iron #1, Dry Sand Rubber Wheel specimen wear scar, 1000X.

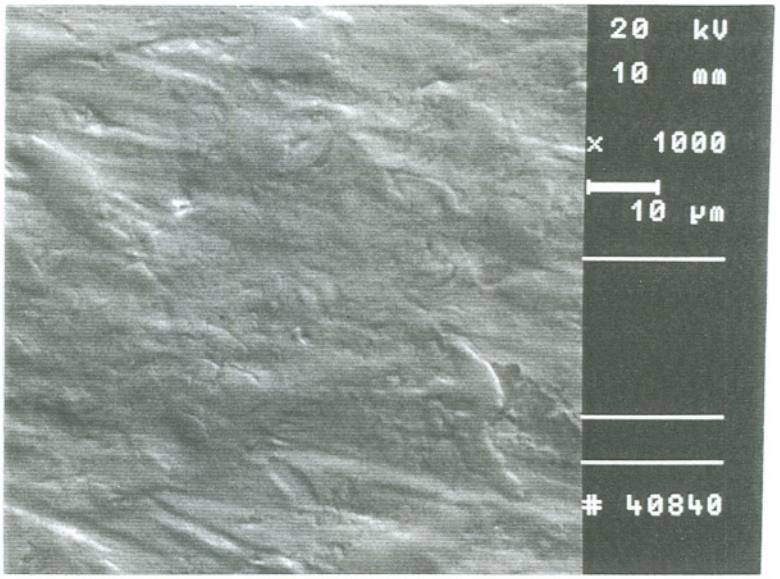

Figure 4.24 Heat treated Cr Iron #2, Dry Sand Rubber Wheel specimen wear scar, 1000X.

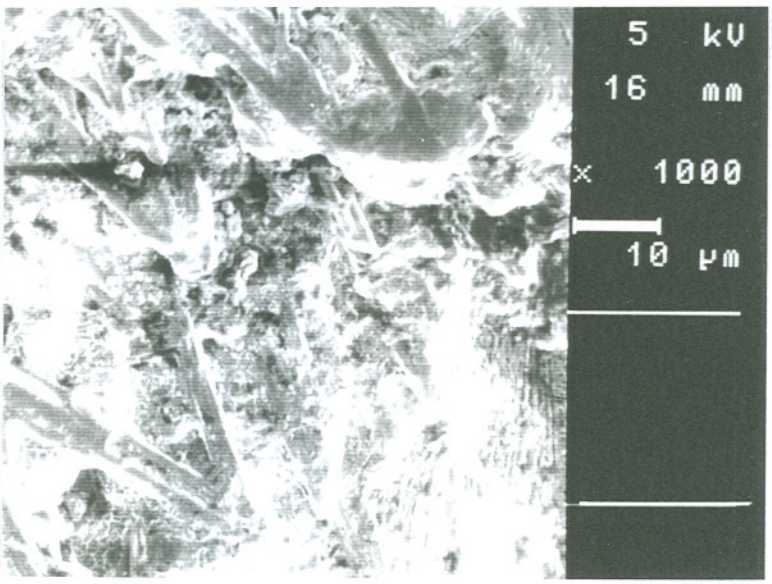

Figure 4.25 Arc-Cr Iron alloy, Dry Sand Rubber Wheel specimen wear scar, 1000X.

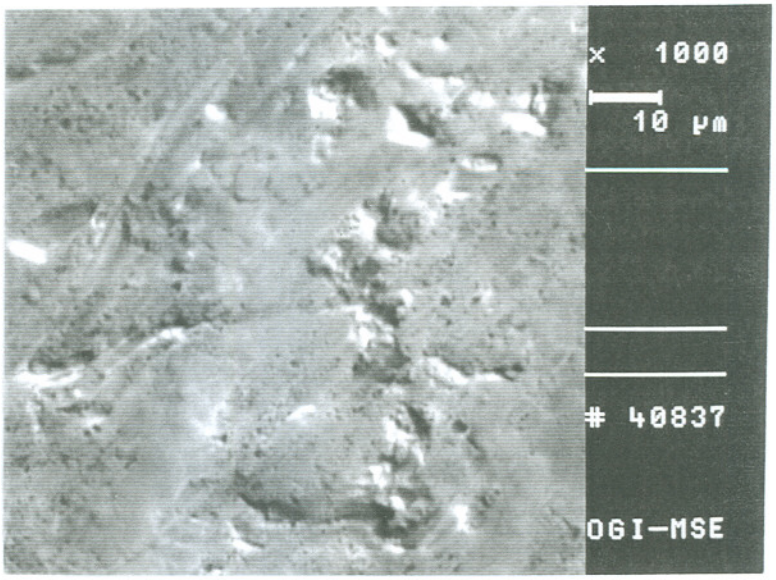

Figure 4.26 440C stainless steel, Dry Sand Rubber Wheel specimen wear scar, 1000X.

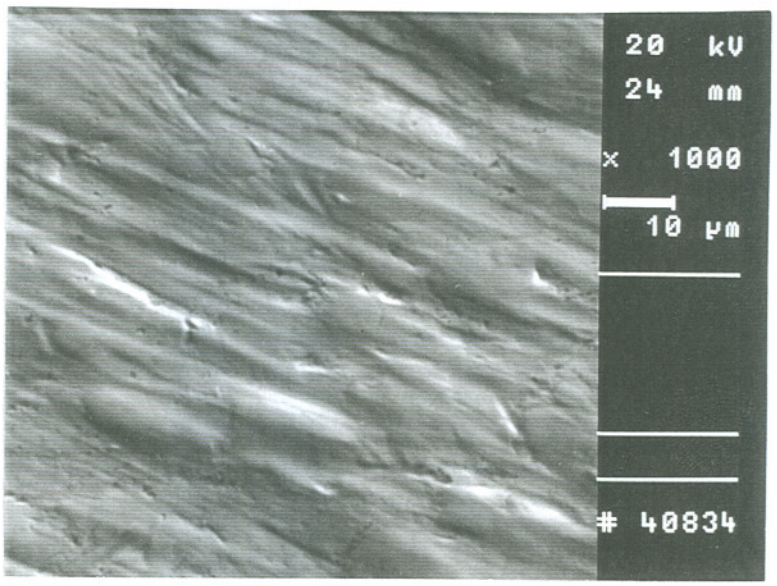

Figure 4.27 D2 tool steel, Dry Sand Rubber Wheel specimen wear scar, 1000X.

CHAPTER 5.
DISCUSSION

5.1 X-Ray Diffraction Analysis

The sample preparation method used in the first diffraction analysis utilized repeated etching and scraping to accumulate material. The scraping presumably removed material which would otherwise have been dissolved. For instance, trace amounts of the α-Fe phase were found in some of the diffraction data which would have normally been dissolved had the etchant been allowed to continue to work uninterrupted and without the mechanical removal. The second analysis method incorporated a much more aggressive electrolytic etch and no mechanical means of material removal. Far fewer compounds were identified from this material. For instance, Alloy #4 exhibited the *R*-phase intermetallic and M_6C carbide in the second X-ray diffraction analysis where the first analysis contained multiple intermetallic and carbidic phases.

The first diffraction data seemed fairly noisy but most of the various phases were readily identified. There was some concern, however, because the powders were sprinkled onto double-sided tape and stuck to a glass slide which was then placed on the goniometer. The potential for misalignment was significant. The powder also had the potential to be non-uniform in size which could have caused some peak broadening [48].

The identification of a primary intermetallic phase in the X-ray diffraction data was a concern through the initial course of this work. Indications from the literature [9] were that the *R*-phase was stable enough to expect its presence in non-equilibrium materials. Initially, no good matches were found by which to identify this phase in these data. This confusion was compounded by the over lapping peaks from other phases. The phase was given in the binary phase diagram [16] as having the Fe_5Mo_3 structure. Both sets of X-ray diffraction data

performed on the experimental alloys showed good matches for the $Fe_{63}Mo_{37}$ which was suspected to be a stoichiometric variation of this primary phase. Similarities were found by comparing the d-spacings from the powder diffraction file for the $Fe_{63}Mo_{37}$ intermetallic to X-ray diffraction data from Sinha's [17] primary *R*-phase, which was designated as having the Fe_5Mo_3 structure. The two structure designations were found to share the same d-spacings and were not the result of having more of one solute available for substitutions during solidification.

Three intermetallic stoichiometries were identified in the X-Ray analysis which included the Fe_2Mo Lavas phase, the μ-phase, and the *R*-phase. The d-spacings for the μ-phase, listed as the Fe_7Mo_6 and Fe_3Mo_2 structures in the literature, are cited [9,17] as being minor derivatives of the same phase. An examination of a crystallographic database [46] confirms that the Fe_3Mo_2 and Fe_7Mo_6 phase designations share the same trigonal crystal structure. The differences are attributed to variability in the stoichiometry of the compounds resulting from substitution of atoms at various lattice sites. No matches for the Fe_7Mo_6 were found in the diffraction results for the experimental alloys.

The matches for the M_6C peaks tended to be very strong. Other carbide structures were less certain, such as the ξ-phase. The tables of X-ray diffraction data in the appendices reveal that several of the sets of peaks are over lapping with other phases resulting in matches that are less distinct. For instance, some of the ξ-phase peaks are similar to those of the Fe_2Mo and *R*-phase intermetallics.

5.2 Metallographic Examination

During solidification, the molybdenum steels pass through an extensive α-Fe phase field, shown on the binary Fe-Mo phase diagram and the ternary Fe-Mo-C liquidus projection, which can absorb up to 30% molybdenum at 1500°C. It then goes through an α-Fe plus μ-phase field. As the temperature decreases, the μ-phase precipitates peritectoidally in the molybdenum saturated α-Fe matrix. As the temperature continues to decrease, the

Fe_2Mo peritectoid begins to precipitate.

The molybdenum steels, Alloys #2, #3, and #4, revealed three distinctly different microstructures. Alloy #2, ferritic with a possible μ-phase dispersed throughout the matrix and on the grain boundaries, Alloy #3, a similar chemistry to Alloy #2 with a much coarser intermetallic dispersion throughout the microstructure, and Alloy #4, containing a high volume fraction primary *R*-phase and M_6C carbide phases. As for intermetallics, the stain reagents on the metallographic specimens are only known to color the Fe_3Mo_2 phase. It is not known if other intermetallics such as the *R*-phase or the Fe_2Mo phases would also be colored. Further, the X-ray diffraction results on the four alloys that were tested, including Alloy #4, indicate that the Fe_2Mo and Fe_3Mo_2 intermetallics are present and stable at room temperature in the experimental alloys.

The microconstituents of Alloys #2 are especially difficult to identify visually. The matrix material is too fine to be resolved but appears to contain at least one secondary phase. This is not a dispersed precipitate which would be expected for a carbide in a low carbon alloy. The only possibilities include the two intermetallics mentioned above, even if the carbon content was several points higher than indicated by the Leco combustion analyzer.

The grain boundary phase visible in Figure 4.2 is still a mystery. The dark staining Murakami's etch in Figure 4.1 identifies the grain boundary material to be an intermetallic or an M_6C carbide. In Figure 4.2, the grain boundary precipitate did not stain at all with the alkaline sodium picrate. The effect of the stain etchants was sometimes found to be variable during the course of this work, but it could also be indicate that the etch was unable to attack the phase as it should because of some contaminant. The grain boundary phase has an obvious depletion zone adjacent to it, indicating a secondary phase which has depleted the neighboring region of molybdenum. The possibilities might include a carbide if the carbon composition was in error. This, along with the obvious microstructural differences between Alloys #2 and #3, might lead to the conclusion that the measured chemistries are in error and a carbide is possible. Even if this were the case, the carbide volume fraction would be insignificant and would probably behave no differently than an intermetallic phase in an abrasive wear environment.

The chemical analysis of Alloy #3 showed it to have a similar composition to Alloy #2. Theoretically it should have a slightly higher carbon content judging from the typical melting losses experienced by the other molybdenum alloys. With losses of approximately 30%, this composition should contain 0.5% carbon. This may be enough carbon in combination with the high molybdenum content to put this alloy into the γ-Fe primary phase field which would then decompose eutectoidially with ξ-phase carbides and ferrite. Murakami's reagent generated a moderate tint indicating ξ-phase while the alkaline sodium picrate gave a much darker shade indicating several possible carbides and the μ-phase intermetallic. Hardness values for Alloy #3 averaged 39 HR_C which is at the high end for a fully pearlitic alloy. This evidence supports the supposition of a eutectoid morphology consisting of the ξ-phase carbide and ferrite. Whatever the composition, the microstructure does have the appearance of a non-uniform eutectoid. Irregardless, the wear rate of 401 *ug/m* may be too high for that of a eutectoid steel. Data from a similar ASTM DSRW test of a series of five wrought 1090 steels produced an average wear rate of 289 *ug/m* with hardness averaging HR_C 27. This wear rate is far lower and with a much softer steel than Alloy#3.

The possibility of Alloy #3 containing intermetallic may be more reasonable. The dark stained phase in Figure 4.3 is most likely the μ-phase and it follows that the slightly delineated, un-stained, material underneath the stained precipitate is the Fe_2Mo intermetallic. This scenario would be in keeping with the measured chemistry for the alloy and is in keeping with the wear rates found for the material.

Alloy #4 contained a significant portion of the primary *R*-phase intermetallic which reveals a distinct decompositional phase. The dark stained microconstituent in Figure 4.4 marks the transformation of the primary *R*-phase by a peritectoid decomposition to the μ-phase in conjunction with α-Fe. This is one of the phases listed as being darkened by the stain reagents. This reaction product can be seen more clearly on the fringes of some of the larger microconstituents in Figure 4.5.

The M_6C carbide also showed a strong presence in Alloy #4 with the X-ray diffraction analysis results. This phase was described by Sato [14] as having a globular appearance but the identification of the phase in the present microstructures has not positively been made. Sato's description was for the secondary carbides that formed in his molybdenum steels and may not be applicable for a primary material. A phase can be seen which has a similar appearance to the chromium carbides found in Cr Iron #1 and #2. In Figure 4.5, this is the finer, interdendritic phase in the micrograph. In the microstructures of Alloys #7 and #8, the primary M_6C exhibits a classic angular dendritic carbide morphology which is very different from this one. Another possibilty is that the phase in question is the decomposition products of the M_6C carbide. The only reaction that would make sense was one described by Schuster [22] as forming α-Fe and Mo_2C at 1190°C in his published reaction sequences. This combination is implausible because the Mo_2C carbide was not found in the X-ray diffraction results. Other phases were found in the X-ray analysis. These included the α-Fe, Fe_2Mo, and the ξ-phase of which none could be specifically related to features in the photomicrographs.

The iron alloys fit into two categories consisting of hypoeutectic and hypereutectic compositions. Alloys #5 and #6, Figures 4.6 and 4.7 repectively, have a classic hypoeutectic dendritic matrix of retained austenite with lath martensite surrounded by a ternary eutectic. No evidence was found indicating that the primary ξ-phase field exists. Alloys #7 and #8, Figures 4.8 through 4.10, exhibit the hypereutectic compositions of primary carbide with eutectic. Evidence of possible decomposition products can be seen in both alloys.

Alloys #7 shows primary M_6C carbide which are the angular dendritic phases darkend by the stain reagent. At the edges of some primary carbides, a decompositional phase appears as a "moat" surrounding the primary M_6C phase. Published solidification sequences show a reaction of M_6C decomposing as a eutectoid-like reaction to Mo_2C but the micrographs reveal the distinct morphology of a peritectic or peritectoid reaction. As this is a primary phase, the moat cannot possibly be the result of a solute depletion zone. Rivlin [9] discussed a possible ternary peritectoid reaction involving Fe_3C, Mo_2C, and γ-Fe to form

Fe_2MoC. Alternatively, Schuster [22] claimed a ternary peritectic with *L*, γ-Fe, and Mo_2C forming the ξ-phase. The evidence here supports Rivlin [9], but, there is enough confusion concerning this portion of the ternary that extensive work would be required to establish the origin of this phase.

Eutectoidal decomposition of some primary carbides can be seen in Alloy #8, Figure 4.10. Here, whole carbides appear to have transformed to what may be the result of the M_6C decomposition to Mo_2C and α-Fe. The Mo_2C carbide was found in the X-ray diffraction data and many of the primary carbides look different from the larger dendritic carbides of Alloy #7. The typical primary carbides of Alloy #8 are smaller and do not have the dendritic appearance.

Alloys #7 and #8 contain 2.7% and 3.0% carbon respectively but Alloy #8 contained less carbide volume fraction than Alloy #7. The differences in chemistry pushed Alloy #7 well within the primary M_6C phase field and created a more hypereutectic composition providing a greater volume fraction of blocky primary carbide. The remaining microconstituents consist of ternary eutectic and α-Fe.

5.3 Analysis of DSRW Specimens

When the DSRW data were viewed relative to the microstructures of the specimens, some insight into the wear mechanisms were furnished. Further verification was provided by an SEM examination of the wear scars on the DSRW specimens to determine the effect of the abrasive on the specimen surfaces. This constituted a simple failure analysis which revealed craters where material was removed from the surfaces, protruding carbides and material plowed and fractured by the abrasive particles.

Alloys #2 and #3 showed the least wear resistance of the experimental molybdenum alloys. They also exhibit worn surfaces very different from each other. Certain areas of the wear scar on the Alloy #2 specimen, Figure 4.16, have had material removed from the surface. These were often elongated pockets which were oriented perpendicular to the wear tracks. Portions of the intermetallic phase may have been plucked from the grain boundaries

to form these features. The grain boundary material may be inclined to fracture and spall under the repeated stress of the passing abrasive particles. The surface of the specimen also presents an impression that a significant amount of plastic deformation has occurred. The ferritic matrix apparently did not gain any support from the intermetallic thought to be present in the matrix. The entire surface of Alloy #3, Figure 4.17, exhibits a rough texture which appears to be the result of small particles having been torn away. These particles fit the size and shape of the hard phase present in the microstructure which are smaller than the wear tracks of the abrasive particles. Occasional craters were found which were elongated in the direction of wear resulting from clusters of hard particles being removed. The craters result from unsupported particles being plucked away from the edges of small pits which eventually becomes a larger crater. This was similar to that described by Desai et al [39].

It would seem that as the wear progressed, eventually the surface of the wear scar would be covered with the larger craters. That this is not the case indicated that the overall wear rate of the surface is high enough to compete with the crater formation process. Based on the experience of others [39,40], the abrasive is able to remove the particles with the wear debris. This wear mechanism was determined to be a major factor in the higher wear rates found in the materials of Desai et al [39] where the carbides were much smaller than the abrasive.

Pockets of material were removed from the surface of the Alloy #4 wear specimen as well. These pockets correspond with the material around the large primary intermetallic phases which are delineated in Figure 4.18 as a result of the abrasion in the material surrounding them. The abrasion was most active in the areas inbetween the larger microconstituents. The metallic material around the intermetallic was heavily abraded and the interfaces between the metal and intermetallic were spalled with many of the features having been extracted. The abraded primary intermetallic surface is relatively smooth and is not protruding as a harder carbide might. Some wearing of the edges of the the primary intermetallic phase can be detected but no obvious errosion or chipping of the leading edges can be seen. Apparently the intermetallic was not able to offer much resistance to the silica abrasive. No other hard phasses were found to protrude above the surface which may

indicate that there was either very little carbide in the alloy or it was small enough that it was easily removed by the larger abrasive.

The eutectic carbide material in Alloys #5 and #6 were not seriously fragmented by the abrasive. Some particle extraction occurred as seen in Figure 4.19. The wear tracks show the abrasive particles plowed through the eutectic and matrix material equally. However, judging from the wear data, the combination of the small amounts of lath martensite and eutectic performed well compared to the softer steels. The eutectic carbides are typically much smaller than the abrasive wear tracks but were obviously concentrated enough that they did not easily yield to the abrasive.

The carbide volume fraction for Alloys #7 and #8 were the highest for all of the alloys tested. This is a result of their hypereutectic microstructures. Alloy #7 was determined to have a greater volume of carbide, yet, a greater wear rate. This situation has been discussed in the literature and attributed to the fracture of the massive primary carbides as in the case of Fulcher et al [34]. Figure 4.21 reveals that this is in fact the difference between the two alloys. The carbides in alloy #8, Figure 4.22, were found intact even though the matrix was eroded away and the carbides were protruding above the surface of the specimen and with some edge rounding.

The as-cast Cr Iron #1, the heat treated Cr Iron #2, and the D2 tool steel, Figure 4.23, 4.24, and 4.27 respectively, were very similar with relatively smooth and intact surfaces. The hard phases can be seen protruding above the surrounding surfaces as a result of erosion of the matrix material. This is especially true with the D2 tool steel and the heat treated Cr Iron #2 where the carbides are readily apparent because of the erosion of the matrix phase surrounding them. Interestingly, the austenitic as cast Cr Iron #1 did not experience the same level of matrix erosion with respect to protruding carbides. It did experience more plowing by the abrasives through the matrix which can develop work hardening in the surface as described by Zum Gahr [34]. The ductility of the austenitic matrix may also have allowed more plowing and limiting the material becoming detached in the form of wear debris.

The wear surface of the Arc-Cr Iron alloy DSRW specimen, Figure 4.25, is of special interest. Here, the fine eutectic carbides are fractured and exposed on the surface of the specimen where the matrix material has been eroded by the abrasives. This is in sharp contrast to the Cr Iron #1 specimen shown in Figure 4.23 where the carbides are intact, slightly rounded and protruding from the surface.

The wear surface of the 440C stainless steel contains obvious cavities where material has been extracted during the course of the abrasive wear, Figure 4.26. It is more difficult to make a microstructural relationship judgment as to the volume of material eliminated when it is most likely portions of the interdendritic eutectic phase being removed rather than individual carbides. The matrix phase is not especially damaged, but, significant plastic deformation has occurred on the surface and the overall wear rate was high.

5.4 Wear Testing

The weight loss versus sliding distance data, Figure 4.12, for the standard commercial chromium alloys are comparable with the results of the most wear resistant experimental molybdenum materials, Alloys #6, #7, and #8, Figure 4.11. The chromium alloys obtain this level of wear resistance with as low as 12% carbide volume fraction while the molybdenum alloys require 30% to 40%. The 20-2-1 white iron alloys are nominally 30% carbide volume fraction in the as cast and heat treated condition. However, the finer microstructure found in the Arc-Cr Iron alloy produced a much higher wear rate. This is strong evidence that the major difference between the molybdenum and chromium white iron materials is the relative size of the microstructural constituents. Hypereutectic chromium compositions were not available for comparison to the hypereutectic molybdenum alloys. The D2 tool steel has a completely different microstructure from any of the other alloys because it is hot rolled and heat treated to develop discrete carbides in a tempered martensitic matrix rather than a cast structure. The wear rate of the chromium irons and the D2 tool steel were indistinguishable.

The insensitivity to wear rate of the chromium alloys with respect to bulk hardness is in direct contrast to the wear behavior of the molybdenum alloys. This is illustrated in Figure 4.13 where the wear rate of the molybdenum materials are linearly dependent on bulk hardness. This demonstrates a commonality between the different materials of each family of alloys. Making the point even stronger is the fact that the chromium alloys and data were obtained from different sources. Fulcher's experimental cast chromium alloys are represented in the data of Figure 4.13. They contain interdendritic hypoeutectic carbides for the carbide volume fraction levels below 30% and primary hypereutectic carbides for the higher carbide volume fraction materials.

Alloy #4 is unique with respect to the other molybdenum alloys because it contains a significant volume fraction of intermetallic phases. The carbide volume fraction is given as 26% with the intermetallic at 33%. There is some doubt in the carbide volume fraction measurement for this relatively low carbon alloy and the microconstituent thought to be the M_6C carbide may not have been a carbide at all. The bulk hardness for the alloy is potentially greater as a result of the presence of the intermetallic. However, the micrographs of the wear specimens representing Alloys #3 and #4 show significant amounts of material pulled from the sufraces. The specimens were apparently not well protected as a result of the presence of the intermetallic. Notwithstanding, the wear data still fits with the other molybdenum alloys on the hardness versus wear rate curve. The 440C steel is also unique in that it produced a much higher wear rate than other materials with similar hardness values.

The wear rate versus carbon content results, Figure 4.14, show the chromium alloys to exhibit very similar behavior to the molybdenum alloys. A second order regression line was fitted for the experimental molybdenum alloy data. The chromium alloys show no relationship of wear rate with carbon content . The 440C stainless steel and the arc melted 20-2-1 white iron are the two outliers on the plot.

The wear rate versus carbide volume fraction data are given in Figure 4.15. The molybdenum alloys are represented by the second order curve fit line. This curve represents the best fit for these data and is consistent with other similar published data in the literature

[39,41]. Fulcher generated a regression curve for his wear data but this is of little significance as the wear rate of these materials show little sensitivity to carbide volume fraction relative to the molybdenum alloys.

Alloy #3 has no carbide but does have a high volume fraction of intermetallic and a high wear rate. The fine dispersed hard phase particles do not offer much resistance to the abrasive particles and the evidence from the failure analysis of the DSRW specimens points to their being easily pulled out of the matrix contributing to the wear rate. This is a condition of the large difference in size between the hard phase and abrasive particles. The hard phase is typically 5 to 10 μm in length while the abrasive is 200 to 300 μm in length and can generate wear tracks of similar size to the hard phase particles.

Alloy #4 did not fit as well with the other molybdenum alloys when plotted with respect to carbide volume fraction. The ideal wear rate should have been 30% lower for a 25% carbide volume fraction alloy, implying that either the small size of the carbides are a factor in its greater wear rate or the supposed carbides were wrongly identified. If this were the case, the carbide volume fraction for this alloy predicted from these data would be far smaller. The data point would fit equally as well on the curve if the carbide volume fraction were to be cut in half.

The wear surfaces show many pockets from extracted particles which appear to have been fractured and removed from around the large primary intermetallic material. The work of Fiore et al [35] showed fracturing of the leading edges of carbides with softer abrasives in DSRW tests. That this was not observed with alloy #4 indicates a relative hardness level between the abrasive and intermetallic that allows the surface to be machined down by the abrasive fast enough that the corners do not become rounded.

Alloy #7 contains larger primary carbides than the other molybdenum alloys yet has a slightly higher wear rate than Alloy #8. This is a direct result of the size of the hypereutectic carbides in the microstructures. This situation has been discussed in the literature [34] and has been attributed to the fracture of the massive primary carbides by the action of the abrasive. The failure analysis on the DSRW specimen provides evidence to

support this contention, Figure 4.22, where an example of a large fractured primary carbide can be seen.

The chromium materials are insensitive to carbide volume fraction except for the 440C steel and the Arc-Cr Iron alloys. The 440C material is notorious for being difficult to heat treat, requiring a double temper to eliminate retained austenite. As a result, it is not fully martensitic and contains fine eutectic carbides which were easily removed from the partially hardened matrix. The greater carbide volume fraction apparently improved the wear rate of the Arc-Cr Iron alloy relative to the 440C steel. However, the wear rate of this material was significantly worse as a result of the arc melt process.

It is obvious that there is a microconstituent size influence on the wear resistance of the white iron alloys. As suggested by Silence [37], after comparing wear rates for his coarse sand cast and finer graphite cast materials, the overall differences between the various groups of alloys are due to the variation in the size of the microstructural constituents. Desai [39] also found a strong correlation with decreasing wear rate and increasing carbide size.

The molybdenum and Arc-Cr Iron alloys of this study have a much finer microstructure due to the small size of the specimens and the water cooled crucible in which they were melted providing a much faster cooling rate. The commercial chromium alloys are very coarse with Fulcher's alloys having the largest microstructure of all. Silence's results showed a slightly softer, coarse structure to be more wear resistant than a finer, harder one. A correlation for wear resistance relative to carbide diameter was ultimately found for the coarse microstructure materials and to a lesser extent for the finer microstructures. The most striking evidence lies with the Cr Iron #1 and the Arc-Cr Iron specimens. The Arc-Cr Iron material was produced by arc melting the exact same material. The difference in wear rate between the two is dramatic and is further confirmation of the importance of the microstructural size.

CHAPTER 6.

CONCLUSIONS

1) The experimental molybdenum steels contained intermetallic phases including the Fe_2Mo Lavas, Fe_3Mo_2 μ-phase, and the primary *R*-phase.

2) Analysis of carbidic phases found in the experimental molybdenum alloys included the M_6C, Mo_2C, and the ξ-phase.

3) Metallography and X-Ray diffraction results identifying phases present in the experimental molybdenum alloys indicate a correlation nearer to that of the ternary system described by Schuster et al.

4) Chromium alloys featuring large coarse carbides exhibited wear rates which were insensitive to carbide volume fraction and bulk hardness. Alloys displaying much finer hard phases showed a relationship of increasing wear resistance and bulk hardness with increasing carbide volume fraction.

5) Carbide size was found to be the dominant factor controlling the wear resistance of the chromium and molybdenum iron alloys. Alloys containing larger carbides showed increased wear resistance.

6) The wear resistance of the intermetallic containing experimental molybdenum steels is significant less than that of the molybdenum or chromium irons containing similar size carbides.

7) The bulk hardness and wear resistance of the alloys is a function of the size and spacing of the hard phases in the surface and is a determinant factor in the ability of a particle to penetrate the matrix. Smaller particles can be pushed into the surface or removed entirely while the larger more closely spaced carbides offer superior protection.

REFERENCES

[1] "A Screening for Potentially Critical Materials for the National Stockpile", Chapter 3 - Chromium, The Report of the Committee on the Technical Aspects of Critical and Strategic Materials, The National Materials Advisory Board, Publication NMAB-329, 1977, 7-18.

[2] M.R. Scholl, "Development of Intermetallic-Hardended Abrasion Resistant Weld Hardfacing Alloys", PhD Dissertation, The Oregon Graduate Center, Department of Materials Science and Engineering, 1986, 1.

[3] National Institute for Occupational Safety and Health, *Material Safety Data Sheet*, "Chromium Metal", February, 1997.

[4] G.V. Samsonov, I.M. Vinitski, *Handbook of Refractory Compounds*, Plenum Publishing Co., New York, N.Y., 1980, 162, 290-295.

[5] R.B. Gundlach, J.L. Parks, "Influence of Abrasive Hardness on the Wear Resistance of High Chromium Irons", *Wear*, Vol 46, No. 1, 1978, 97-108.

[6] W. Fairhurst, K. Rohrig, "Abrasion Resistant High-Chromium White Cast Irons", *Foundry Trade Journal*, May, 1974, 685-698.

[7] *Smithells Metals Reference Book*, 7th Edition, E.A. Brandes, G.B. Brook, Editors, Butterworth-Heinemann LTD Publishing, London, 1992, **27**-3.

[8] M.G. Manzone, J.Z. Briggs, *Less-Common Alloys of Molybdenum*, Climax Molybdenum Co., New York, 1962, 35-43.

[9] V.G. Rivlin, "Phase Equilibria in Iron Ternary Alloys, 17: Critical Review of the Constitution of the Carbon-Iron-Molybdenum Systems", *International Metals Reviews*, Vol 30, No. 3, 1985, 109-124.

[10] D.J. Dyson, K.W. Andrews, "The Structure and Metallurgical Significance of the Iron-Molybdenum Carbide Fe_2MoC (M_aC_b)", *Journal of the Iron and Steel Institute*, April, 1964, 325-329.

[11] K. Kuo, "Carbides in Chromium, Tungsten, and Molybdenum Steels", *Journal of the Iron and Steel Institute*, April, 1953, 363-375.

[12] K. Kuo, "The Formation of η-Carbides", *Acta Metallurgica*, Vol. 1, May, 1953, 301-304.

[13] R.F. Cambell, S.H. Reynolds, L.W. Ballard, K.G. Caroll, "Constitution of Fe-C-Mo Alloys Containing 0.05-1.3 pct C and 0.03-6.0 pct Mo", *Transactions of the Metallurgical Society of the American Institute of Mechanical Engineers*, Vol. 218, 1960, 723-733.

[14] T. Sato, T. Nishizawa, K. Tamaki, "Carbides in Molybdenum Steels", *Transactions of the Japanese Institute of Metals*, Vol. 3, 1962, 196-202.

[15] A.C. Fraker, H.H. Stadelmaier, "The Eta Carbides of Molybdenum-Iron, Molybdenum-Cobalt, and Molybdenum-Nickel", *Transactions of the Metallurgical Society of the American Institute of Mechanical Engineers*, Vol. 245, 1969, 847-850.

[16] *Binary Phase Diagrams*, Volume 2, Second Edition, T.B. Massalski, Editor, The American Society of Materials, Materials Park, Ohio, 1990, 1727.

[17] A.K. Sinha, R. A. Buckley, W. Hume-Rothery, "Equilibrium Diagram of the Iron-Molybdenum System", *Journal of the Iron and Steel Institute*, 1967, Vol. 205, 191-195.

[18] Y.Komura, W.G. Sly, D.P. Shoemaker, "The Crystal Structure of the R-Phase, Mo-Co-Cr", *Acta Crystallographica*, Vol. 13, 1960, 575-585.

[19] C.P. Heijwegen, G.D. Rieck, "Determination of the Phase Diagram of the Mo-Fe System Using Diffusion Couples", *Journal of the Less-Common Metals*, Vol. 37, No. 1, 1974, 115-121.

[20] T. Nishizawa, "Thermodynamic Study of the Fe-Mo-C System at 1000°C", *Scandinavian Journal of Metallurgy*, Vol. 1, 1972, 41-48.

[21] J. Andersson, "A Thermodynamic Evaluation of the Fe-Mo-C System", *Calphad*, Vol. 12, No. 1, 1988, 9-23.

[22] J.C. Schuster, H. Nowotny, H. Ipser, H. Gupta, "The Constitution of the Ternary System Iron - Molybdenum - Carbon", *Zeitschrift fur Metalkunde*, Bd. 82, H. 7, 1991, 539-543.

[23] *Metals Handbook*, 8th Edition, Vol 8, American Society for Metals, Metals Park, Ohio, 1973, 408-411.

[24] P. Leckie-Ewing, "A Study of the Microhardness of the Major Carbides in Some High Speed Steels", *Transactions of the American Society of Metals*, Vol. 44, 1952, 349-366.

[25] D. Dowson, *History of Tribology*, Longman Group Limited, London, 1979, 499.

[26] R. Blickensderfer, B.W. Madsen, J.H. Tylczak, "Comparison of Several Types of Abrasive Wear Tests", *Proceedings of the International Wear of Materials Conference*, Vancouver, B.C., Canada, American Society of Mechanical Engineers, New York, 1985, 313-323.

[27] H.S. Avery, "Classification and Precision of Abrasion Tests", *Proceedings of the International Wear of Materials Conference*, St. Louis, Missouri, The American Society of Mechanical Engineers, New York, 1977, 148-157.

[28] H.S. Avery, "The Nature of Abrasive Wear", *Society of Automotive Engineers Publication #750822*, 1975, 1-15.

[29] *Treatise on Materials Science and Technology*, Vol. 13, D. Scott, Editor, Academic Press, New York, 1979, 221-222.

[30] *Wear Control Handbook*, M.B Peterson, W.O. Winer, Editors, Sponsored by the Research Committee on Lubrication, American Society of Mechanical Engineers, New York, 1980, 65-67.

[31] E. Rabinowicz, *Friction and Wear of Materials*, Second Edition, Wiley and Sons, New York, 1995, 192-194.

[32] A. Misra, I. Finnie, "On the Size Effect in Abrasive and Erosive Wear", *Wear*, Vol. 65, No. 3, 1981, 359-373.

[33] J.K. Fulcher, T.H. Kosel, N.F. Fiore, "The Effect of Carbide Volume Fraction on the Low Stress Abrasion Resistance of High Cr-Mo White Cast Irons", *Wear*, Vol. 84, No. 2, 1983, 313-325.

[34] K.H. Zum Gahr, G.T. Eldis, "Abrasive Wear of White Cast Irons", *Wear*, Vol. 64, No. 1, 1980, 175-194.

[35] N.F. Fiore, J.P. Coyle, S.P. Udvardy, T.H. Kosel, W.A. Konkel, "Abrasive Wear-Microstructure Interactions in a Ni-Cr White Iron", *Wear*, Vol. 62, No. 2, 1980, 387-404.

[36] K.H. Zum Gahr, "Abrasive Wear of Two-Phase Metallic Materials with a Coarse Microstructure", *Proceedings of the International Wear of Materials Conference*, Vancouver, B.C., Canada, American Society of Mechanical Engineers, New York, 1985, 45-58.

[37] W.L. Silence, "Effect of Structure on Wear Resistance of Co-, Fe-, and Ni-Base", *Proceedings of the International Wear of Materials Conference*, Vancouver, B.C., Canada, American Society of Mechanical Engineers, New York, 1985, 77-85.

[38] W.P. Leech, "High Stress Abrasion of Carbidic Hardfacing Alloys", *Surface Engineering*, Vol. 5, No. 1, 1989, 41-44.

[39] V.M. Desai, C.M. Rao, T.H. Kosel, N.F. Fiorie, "Effect of Carbide Size on the abrasion of Cobalt-Based Powder Metallurgy Alloys", *Wear*, Vol. 94, No. 1, 1984, 89-101.

[40] T. Kulik, T.H. Kosel, "Effects of Second Phase Particle Size and Edge Microfracture on Abrasion of Model Alloys", *Proceedings of the International Wear of Materials Conference*, Denver, Colorado, Vol. I, The American Society of Mechanical Engineers, New York, 1989, 71-81.

[41] T.H. Kosel, S.Z. Li, C.M. Rao, "The Size Effect in Abrasion of Dual-Phase Alloys", *Transactions of the American Society of Lubrication Engineers*, Vol. 8, No. 3, 1965, 343-350.

[42] G. Huard, J. Masounave, M. Fiset, Y. Cote, D. Noel, "The Effects of Size and Shape of Abrasive Particles on the Measurement of Wear Rate Using a Dry Sand Rubber Wheel Test", *Proceedings of the International Wear of Materials Conference*, Houston, Texas, American Society of Mechanical Engineers, New York, 1987, 689-699.

[43] A. Misra, I. Finnie, "Correlations between Two-Body and Three-Body Abrasion and Erosion of Metals", *Wear*, Vol. 68, No. 1, 1981, 33-49.

[44] W. Rostoker, J.R. Dvorak, *Interpretation of Metallographic Structures*, Second Edition, Academic Press, New York, 1977, 147.

[45] *Powder Diffraction File*, "Inorganic", American Society for Testing and Materials, Philadelphia, PA, 1967.

[46] P. Villars, L.D. Calvert, *Pearson's Handbook of Crystallographic Data for Intermetallic Phases*, Vol. 3, American Society of Metals, Metals Park, Ohio, 1989, 2193-2194.

[47] *X-Ray Powder Diffraction File*, Joint Center for Powder Diffraction Files, International Center for Diffraction Data, Newton Square, PA, 1994.

[48] B.D. Cullity, *Elements of X-ray Diffraction*, Second Edition, Addison-Wesley, Reading, Mass, 1978, 99-106.

APPENDIX

X-Ray Diffraction Data

First Data Analysis

Alloy #4: α-Fe

Powder Diffraction File		Measured Peaks	
d-Spacing	I (%)	d-Spacing	I (%)
2.026	100%	2.026	32%
1.433	20%	1.447	26%
1.170	30%	1.173	57%

Alloy #4: Fe_3Mo_2

Powder Diffraction File		Measured Peaks	
d-Spacing	I (%)	d-Spacing	I (%)
3.46	8	3.468	20
2.37	90	2.357	24
2.18	65	2.178	38
2.08	100	2.076	32

Alloy #4: Fe_2Mo

Powder Diffraction File		Measured Peaks	
d-Spacing	I (%)	d-Spacing	I (%)
2.36	60	2.355	24
2.18	100	2.180	40
2.05	60	2.066	29
2.02	100	2.026	31
1.98	60	1.973	28
1.365	60	1.358	26

Alloy #4: $Fe_{63}Mo_{37}$

Powder Diffraction File		Measured Peaks	
d-Spacing	I (%)	d-Spacing	I (%)
2.343	20	2.346	25
2.181	100	2.178	41
1.963	50	1.963	47
1.891	20	1.899	27
1.304	10	1.306	60
1.272	40	1.278	58
1.230	20	1.231	57
1.114	70	1.116	55
1.075	20	1.075	60

Alloy #4: Fe_3Mo_3C

Powder Diffraction File		Measured Peaks	
d-Spacing	I (%)	d-Spacing	I (%)
2.760	25	2.774	32
2.530	40	2.548	30
2.260	65	2.266	40
2.130	100	2.140	100
1.955	40	1.964	36
1.306	45	1.309	55
1.116	13	1.117	55
1.088	9	1.089	57
1.074	8	1.075	57

Alloy #4: $Fe_{11}Mo_6C_5$

Powder Diffraction File		Measured Peaks	
d-Spacing	I (%)	d-Spacing	I (%)
2.348	60	3.355	24
2.293	60		
2.279	60	2.268	53
2.087	100	2.074	32

Alloy #5 α-Fe

Powder Diffraction File		Measured Peaks	
d-Spacing	I (%)	d-Spacing	I (%)
2.026	100	2.018	100
1.433	20		
1.170	30	1.168	85

Alloy #5: Mo_2C

Powder Diffraction File		Measured Peaks	
d-Spacing	I (%)	d-Spacing	I (%)
2.28	100	2.256	62

Alloy #7: Fe_3Mo_3C

Powder Diffraction File		Measured Peaks	
d-Spacing	I (%)	d-Spacing	I (%)
2.530	40	2.548	21
2.260	65	2.271	100
1.113	13	1.111	68
1.088	9	1.109	65
1.074	8	1.068	100
1.069	2	1.062	53

Alloy #7: Mo_2C

Powder Diffraction File		Measured Peaks	
d-Spacing	I (%)	d-Spacing	I (%)
2.60	20	2.592	30
2.37	30	2.358	30
2.28	100	2.271	100

Alloy #7: Fe_2MoC

Powder Diffraction File		Measured Peaks	
d-Spacing	I (%)	d-Spacing	I (%)
2.618	10	2.592	34
2.477	10	2.471	10
1.344	40	1.354	30

Alloy #8 α-Fe

Powder Diffraction File		Measured Peaks	
d-Spacing	I (%)	d-Spacing	I (%)
2.026	100	2.030	100
1.433	20	1.434	18
1.170	30	1.170	14

Alloy #8: Mo_2C

Powder Diffraction File		Measured Peaks	
d-Spacing	I (%)	d-Spacing	I (%)
2.60	20	2.599	39
2.37	30	2.360	20
2.28	100	2.278	100

Alloy #8: Fe_3Mo_3C

Powder Diffraction File		Measured Peaks	
d-Spacing	I (%)	d-Spacing	I (%)
1.069	2	1.068	100

BIOGRAPHICAL NOTE

The author was born on May 22, 1954 in Olympia Washington and grew up living in various cities in Washington, California, and South Carolina. However, Bellevue, Washington was always considered home and where the author attended High School. After several years of employment at the Boeing Company in Seattle, the author resolved to pursue a career in engineering and attended Washington State University where a degree in Physical Metallurgy was obtained in 1981. This led to positions at the Hanford Nuclear Reservation and then the Oregon Graduate Center as a Research Engineer in 1984 where he eventually began working towards a part-time masters degree. The author left the renamed Oregon Graduate Institute in 1995 as a Senior Research Engineer for a position at ESCO Corporation, Portland, Oregon, in the Metallurgical Laboratory. The requirements for a Master of Science Degree were completed in May 1997.